COMPUTATIONAL APPROACHES TO THE STUDY OF THE ELECTRONIC PROPERTIES, STRUCTURE AND FUNCTIONALIZATION OF METAL NANOPARTICLES

DANIELE RAPETTI

Dipartimento di Chimica e Chimica Industriale
Università degli Studi di Genova

31 May 2021

SUPERVISORS:
    Giulia Rossi
    Riccardo Ferrando
    Arnaldo Rapallo

Daniele Rapetti: *Computational approaches to the study of the electronic properties, structure and functionalization of metal nanoparticles*

SUPERVISORS:
Giulia Rossi
Riccardo Ferrando
Arnaldo Rapallo

PUBLICATIONS

- Daniele Rapetti and Riccardo Ferrando. "Density functional theory global optimization of chemical ordering in AgAu nanoalloys." In: *Journal of Alloys and Compounds* 779 (Mar. 2019), pp. 582–589. ISSN: 09258388. DOI: 10.1016/j.jallcom.2018.11.143. URL: https://doi.org/10.1016/j.jallcom.2018.11.143%20https://linkinghub.elsevier.com/retrieve/pii/S092583881834266X

- Jérome Pirart et al. "Reversed size-dependent stabilization of ordered nanophases." In: *Nature Communications* 10.1 (Dec. 2019), p. 1982. ISSN: 2041-1723. DOI: 10.1038/s41467-019-09841-3. URL: http://www.nature.com/articles/s41467-019-09841-3

- Ali Kemal Garip et al. "A DFT study of chemical ordering and oxygen adsorption in AuPtPd ternary nanoalloys." In: *Materials Today Communications* 25.May (Dec. 2020), p. 101545. ISSN: 23524928. DOI: 10.1016/j.mtcomm.2020.101545. URL: https://doi.org/10.1016/j.mtcomm.2020.101545%20https://linkinghub.elsevier.com/retrieve/pii/S2352492820325563

- Daniele Rapetti et al. "Development of a classical Au-S potential for the simulation of thiol diffusion on gold surfaces"

- Daniele Rapetti and Riccardo Ferrando. "A new Basin Hopping algorithm for the global optimization of nanoalloys"

[...] Having thus threatened the ogre, the young prince fitted to his bow an arrow steeped in deadly poison and let fly. It stuck right in the ogre's hair. Then he let fly, one after another, fifty arrows. All stuck right to the ogre's hair. The ogre shook off every one of those arrows, letting them fall right at his feet, and approached the young prince. Prince Five-weapons threatened the ogre a second time, and drawing his sword, delivered a masterly blow. The sword, thirty-three inches long, stuck right to the ogre's hair. Then the prince smote him with a spear. That also stuck right to his hair. Perceiving that the spear had stuck, he smote him with a club. That also stuck right to his hair. [...], with a yell he struck the ogre with his right hand. His hand stuck right to the ogre's hair. He struck him with his left hand. That also stuck. He struck him with his right foot. That also stuck. He struck him with his left foot. That also stuck. Thought he: "I will beat you with my head and pound you into powder and dust!" He struck him with his head. That also stuck right to the ogre's hair. [...]

— The "Sticky Hair Monster and the Five-weapon Prince" myth retold in "*The Hero With A Thousand Faces*" by Joseph Campbell

ACKNOWLEDGMENTS

Ciao
Un irrituale Daniele

CONTENTS

LIST OF FIGURES

LIST OF TABLES

ACRONYMS

NP   nanoparticle

OP   Order Parameter

PAW   Projector Augmented Wave

PSO   Particle Swarm Optimization

BH   Basin Hopping

LJ   Lennard–Jones

SMATB   Second–Moment Approximation to the Tight–Binding

DFT   Density Functional Theory

HK   Hohenberg and Kohn

PES   potential energy surface

LDA   Local Density Approximation

GGA   Generalized–Gradient Approximation

PBE   Perdew–Burke–Ernzerhof

PAW   Projector Augmented Wave

QE   Quantum ESPRESSO

MD   molecular dynamics

TO   truncated octahedron

Ih   icosahedron

Dh   decahedron

fcc   face centered cubic

bcc   body centered cubic

hcp   hexagonal close–packed

DFTB   Density Functional based Tight Binding

TB   tight–binding

OPLS   Optimized Potentials for Liquid Simulations

Part I

INTRODUCTION

INTRODUCTION

In the last decades [1–3], the interest in nanoparticles (NPs) has grown significantly both in basic and in applied science. On the one hand, understanding and predicting the structures and properties of NPs is a challenging and very interesting problem in basic science, with interdisciplinary aspects which range from physics to chemistry, and materials science. On the other hand, NPs find uses in several fields, including catalysis [3], engineering of nanostructured materials [4], data storage [5] and medicine, both for diagnosis and therapy [1, 2, 6–12].
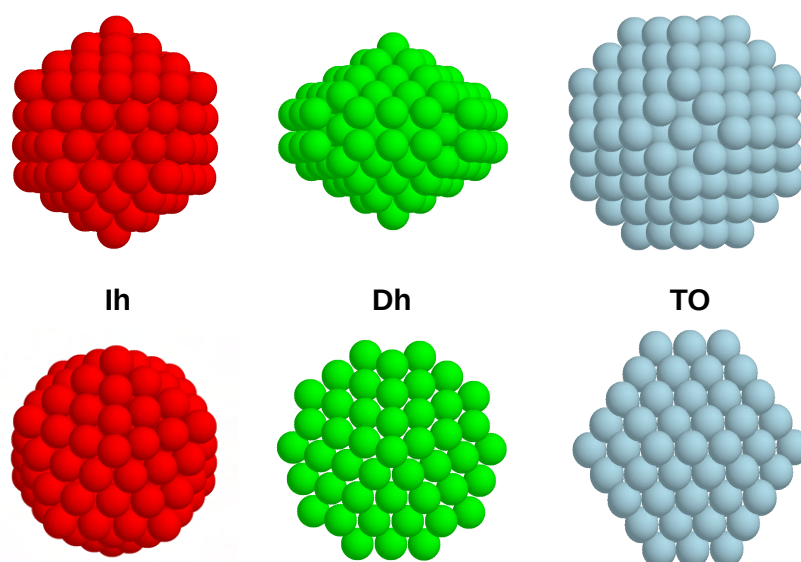
Figure 0.1: Various shapes of nanoparticles: from left to right an icosahedron (Ih), a decahedron (Dh) and a truncated octahedron (TO).

Metal NPs may be composed of atoms of a single species (*elemental nanoparticles*), or they may contain atoms of different species. In the latter case they are called *alloy nanoparticles* or *nanoalloys* [13]. The presence of different metals in the same NP can improve its properties, for example allowing the synthesis of nanomagnets with better magnetic anisotropy, of more efficient nanocatalysts for chemical reactions, and NPs with tunable surface plasmon resonance [14]

While the structure of an elemental NP is determined by its geometric shape [15, 16], the structure of a nanoalloy needs to be characterized also by its chemical ordering, i. e. by the pattern in which the different species are ordered in the NP. Geometric structures can be fragments of the bulk lattice crystal of the metal (such as octahedra, truncated octahedra, tetrahedra) or non crystalline structures, such as icosahedra or decahedra, see fig. 0.1. The latter present fivefold symmetry axes that are not compatible with the translational symmetry of a Bravais lattice.

Chemical ordering can be intermixed (as in solid solutions or intermetallic compounds) or phase-separated (as in core-shell, multi-shell and Janus particles) [13], see fig. 0.2.

Random solution   Ordered alloy   Core-shell

Three- or multi-shell   Janus
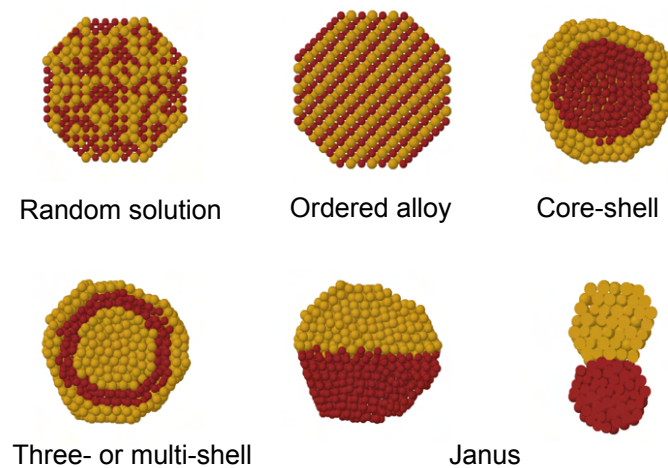
Figure 0.2: Multicomponent nanoparticles can present various chemical ordering.

In this Thesis, I will study different aspects of the structures of NPs from a computational point of view. In this field, theory and simulation results have been often very useful in interpreting existing experiments and in suggesting new ones [15]. This is especially true in the study of NP structures, because of the enormous variety of possible geometric shapes, and, in nanoalloys, of possible chemical orderings.

My aim will be to develop new computational methods for studying NP structures and to apply them to different systems of interest in the field. In one case, the work has been done in direct collaboration with an experimental group. During

my PhD work, I pursued two main objectives, as described in the following sections. The first the global optimization of the structure and chemical ordering of metal nanoalloys. The second is the development of a classical potential for Au-S interactions.

GLOBAL OPTIMIZATION OF NANOALLOY STRUCTURE AND CHEMICAL ORDERING

The first problem I will tackle is the *global optimization* problem of nanoalloys [14, 17]. This problem consists in finding the lowest-energy structure of a nanoalloy given its composition. This requires that both the geometric structure of the nanoalloy and its chemical ordering are optimized together. The importance of solving this problem originates from the fact that the lowest-energy structure corresponds to the thermodynamic equilibrium structure for sufficiently low temperatures. For metal NPs these temperatures may well extend to room temperature and above [18].

The global optimization problem is extremely complex so that it requires the development of specific algorithms. In my thesis, I worked on different aspects of the global optimization problem. These aspects are summarized in the following points:

- In our group, a computer code based on the Basin Hopping (BH) algorithm [19], was already available [20, 21]. That code was written in FORTRAN 90 and lacks any interface with packages for Density Functional Theory (DFT) calculations. My first task has been to rewrite the code in C++ language, also improving its flexibility and speed.

- The new C++ code, called *BH++*, was then interfaced with Density Functional Theory (DFT) packages such as Quantum ESPRESSO [22] and CP2K [23].

- In the framework of a collaboration with the experimental group of Pascal and Caroline Andreazza of the University of Orléans (France), the DFT-BH++ code was used to optimize the chemical ordering of AgPt nanoalloys in vacuum. Our computational results agreed well with the experimental data. This work is published in an article in Nature Communications [24].

- A new algorithm was developed and implemented in BH++. This algorithm is called *BH-F/L*, where F/L stands

for Flying Landing. This algorithm aims at a more efficient simultaneous optimization of geometric shape and chemical ordering in nanoalloys. The new BH-F/L algorithm was tested against a few benchmarks (optimization of AuCu and AuRh nanoalloys for size 400 atoms) with very good results. An article on BH-F/L is in preparation.

DEVELOPMENT OF A CLASSICAL POTENTIAL FOR THE Au−S INTERACTION

A second part of the Thesis is devoted to the development of atomistic force fields to study the interaction between gold and sulphur. In fact, organic and inorganic NPs have a huge impact on modern medicine, despite the fairly short history of nanomedicine [8–10, 25]. In this field, Au NPs covered by thiolated ligands are among the most studied systems.

Au is considered to be easy to functionalize (often via covalent linking of thiolated molecules). The choice of a proper organic coating (that is often called surface functionalization) can improve other characteristics of the NP besides the biocompatibility [26], such as solubility[27] and target selectivity. The functionalization of the NPs can be exploited to store drugs and deliver them in the right place, with the right stimuli.[6, 7, 28]

From the computational point of view, the study of complex systems such as functionalized Au NPs can be made at different levels, corresponding to different size and time scales. The smallest scale is that of electronic structure calculations by *ab initio* methods, such as DFT calculations. These calculations have been used in the first part of my thesis when searching for the equilibrium structures of small metallic NPs in vacuum, but they are not sufficient for studying dynamical phenomena on relatively long time scales (i.e. above a few nanoseconds). Longer time scales may be necessary even to study elementary diffusion processes of molecules on metal surfaces. Moreover, DFT calculations are nowadays limited to the study of rather small systems, up to ∼ 10^3 atoms, which are insufficient when dealing with biological problems.

However, the accurate DFT energetics can be used as a basis to develop simpler models such as atomistic force fields. In atomistic force fields, the electrons are not explicitly treated, but their effect is taken into account by terms that describe the interaction between atoms. Atomistic force fields allow simulating quite

large systems (even with $10^5 - 10^6$ atoms) by molecular dynamics (MD), on time scales extending up to several microseconds.

In my Thesis, I adopted this approach to develop a model for the interaction of thiols with Au crystal surfaces. Thiols are very often used to functionalize Au NPs [29, 30]. They bind to Au surfaces by their sulphur atoms which strongly interact with gold. In my Thesis, I tackled this problem by the following steps

- I made a thorough study of the adsorption of thiols on Au(111) and Au(100) crystal surfaces by means of DFT calculations. These calculations have been used to build a database to be used for fitting the atomistic force field.

- I implemented in LAMMPS [31] the reliable atomistic force field of the Gupta type [32] for Au−Au interactions.

- I developed a bond-order atomistic force field for the Au-S interaction on the basis of the DFT calculations. I also implemented this potential in LAMMPS, where the interactions between S, Au an the other atoms of the thiol have been modelled by the Optimized Potentials for Liquid Simulations (OPLS) force field [33].

- The atomistic force fields contains several parameters. I determined them by minimizing an error function using the DFT data as target. The minimization of this function of several variables was done by the Particle Swarm Optimization (PSO) algorithm [34], which is an heuristic global optimization algorithm well suited to minimize this type of function. I took care both of the PSO implementation and use.

- I tested the force field by making Molecular Dynamics of the simulation of thiols on high-index Au surfaces with satisfactory results.

OUTLOOK

The Thesis is organized as follows

- The first three chapters are dedicated to the tools used in this Thesis:

    - Chapter 1 introduces two global optimizations methods: the Basin Hopping (BH) and the Particle Swarm Optimization (PSO), with an insight on the variations

and on the algorithms of the first and with a description of the reasoning behind the second.

– Chapter 2 formally introduces the Density Functional Theory (DFT) and the calculation methods implied by this *ab–initio* formulation. It also presents a brief history of pseudopotentials.

– Chapter 3 introduces the classical potential used: the Second Moment Approximation to the Thigh binding, used to model the metal-metal interactions, and the OPLS forcefield used to model the organic part of our simulations.

• The last three chapter are dedicated to the results obtained during the work for this Thesis:

– Chapter 4 presents our results on the improvement of our BH code. Here we present our new *BH++* with its improvements over the old code, and we propose a new algorithm for optimizing multicomponent NPs, the BH-F/L.

– Chapter 5 presents our contribution to the study of the formation of the L1$_1$ phase in AgPt NP. We present the experimental results and the Monte Carlo analysis from our collaborators and describe in detail the DFT calculations that we executed.

– Chapter 6 presents the development of the AuS interaction potential. From DFT data of methane thiolate on gold surfaces we derive the form of the potential, we fit the functional form from the DFT data and we present some preliminary result of the MD simulations

Part II

METHODS

GLOBAL OPTIMIZATION

Finding a the lowest minimum of a function of many variables is known as the *global optimization* problem. This problem is encountered in many scientific disciplines [17]: for example in training an artificial intelligence in a specific task, in finding the best configuration for a complex molecule such as a protein, in determining the lowest-energy configuration of a nanoparticle or in fitting complex functions on datasets. In the following we will focus first on the global optimization of the potential energy surface (PES) which is the potential energy of an nanoparticle as a function of the coordinates of its atoms.

The main difficulty in optimizing the PES is that in our cases of interest it presents a huge number of locally stable configurations (the *local minima*), which should in principle be completely explored to find the truly optimal atomic configuration. In general, the number of local minima increases very rapidly with the number of degrees of freedom. In the case of elemental NPs, it has been shown that the increase is exponential (see for example [35] and references therein), so that in a NP of 55 atoms the number of local minima largely exceeds 10^{10}. This means that the exhaustive sampling of all minima is not possible already for such relatively small sizes, even when simple atomistic force fields are used to treat the interactions between atoms. Following this line of reasoning, one may think that the global optimization problem is intractable. However, this is not true, because for non-glassy systems, in which the potential energy function is organized in *funnels* [17], the search for very-low energy configurations can be quite successful.

Several types of algorithms have been developed to tackle this problem in order to search for global minima. Some algorithms take inspiration from natural processes (like simulated annealing, and evolutionary algorithms) other are inspired by equilibrium thermodynamics considerations (such as the Basin Hopping).

In the following, I will present two different optimization algorithms that I used in this PhD Thesis.

1.1 BASIN HOPPING

Basin Hopping is a deformation method, it remaps the function f to be optimized to another function $\tilde{f}$ in order to simplify the optimization procedure. BH in particular remaps each point of the domain of f to the nearest local minimum so that $\tilde{f}$ takes the form of a multi-dimensional staircase function:

$$\tilde{f}(x) = \min_{loc}(f(x)), \tag{1.1}$$

where x belongs to the domain of f.

This kind of remapping has two main advantages: the first is that the $\tilde{f}$ and f present the same minima (same energy, same location), and in particular they share the global minimum; the second is that the landscape of $\tilde{f}$ is somehow simpler to explore. Since $\tilde{f}$ is a staircase (Figure 1.1), it is not derivable, so that directly exploring $\tilde{f}$ by molecular dynamics, which requires the calculation of forces, is not possible. Therefore we need some specific methods to explore this staircase function.
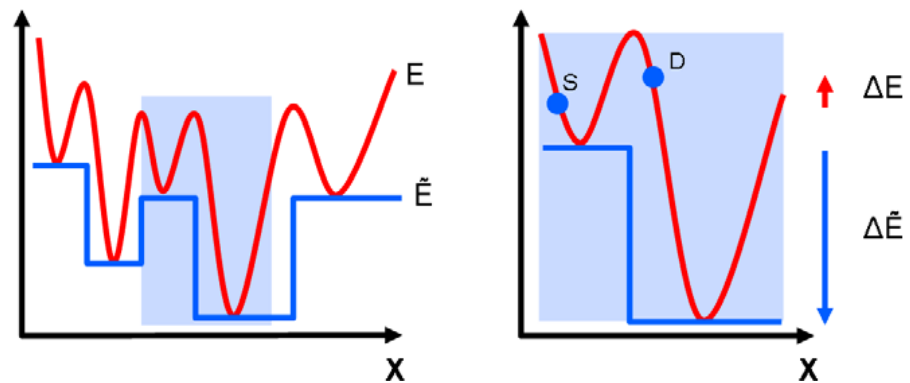
Figure 1.1: An example of the deformation of the function in one dimension. The local minima of f and $\tilde{f}$ have the same values.

Specifically, $\tilde{f}$ is explored with a Monte Carlo procedure. A Monte Carlo procedure consists of several steps. At each step, an elementary move is attempted to reach a new position in the domain of $\tilde{f}$. The move should be calibrated in such a way that it will end in a different minimum than the present one with high probability. The move is either accepted or refused according to a probabilistic criterion.

1.1.1 *Basin hopping in metallic nanoparticles and order parameters*

In the use of the BH algorithm to optimize metallic NPs [21] the moves used to explore the energy landscape are of two kinds: geometric moves, and chemical ordering moves.

Geometric moves are efficient in changing the shape of the NP and combined with the local minimization tend to produce new cluster shapes. Geometric moves can displace all atoms in the cluster by trying to change the overall shape of the NP or they can displace few atoms at a time to cure localized geometric defects of the cluster, such as isolated adatoms on the cluster surface or incomplete facets.

The most common geometric moves for changing the overall shape of a cluster are the *shake* and the *Brownian* move [35]. In the shake move, all atoms are randomly displaced within a sphere centered on their present position. The radius of the sphere is typically half of the nearest-neighbour distance between the atoms. In the Brownian move, a short molecular dynamics run is performed at high temperature. The Brownian move has the advantage of producing physically meaningful configurations, because the disordering of the cluster follows the physical forces. However, it is more expensive than the shake move from the computational point of view. Other shape-changing moves, such as the *bonds* move [35], aim at eliminating defects in the cluster surface.
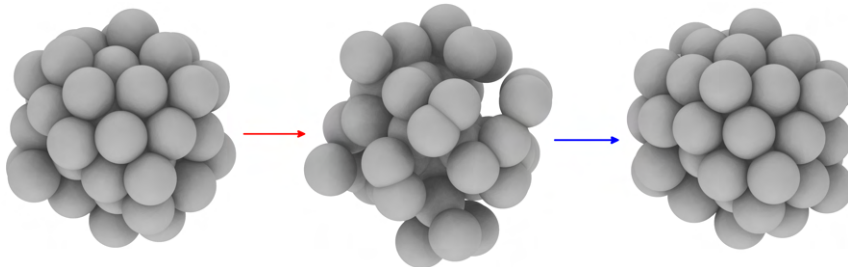
Figure 1.2: A geometric move has a big impact on the structure. In the image from left to right we have the starting configuration, the result of the move and the minimized configuration that will be evaluated by the algorithm.

Chemical ordering moves are less perturbing on the NP and usually consist in exchanging the chemical species of a pair of unlike atoms. The chemical moves are necessary for efficiently optimize the chemical ordering of the NP, helping to optimize separated phases or mixed alloys. Chemical ordering moves can

be tuned to favour the exploration of mixed alloys or to separate the different species in the NP [36, 37].
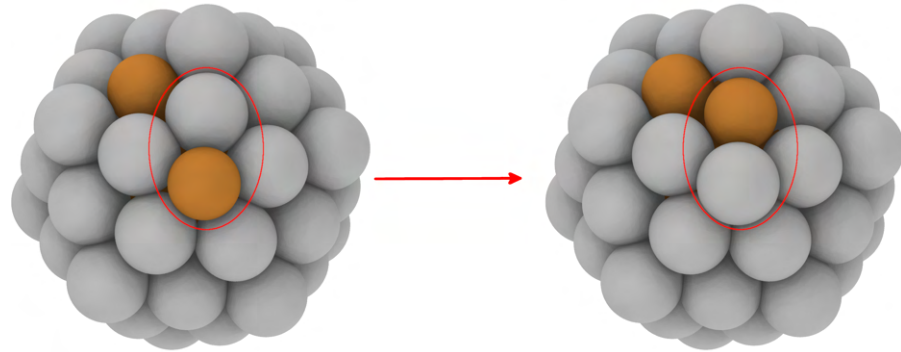
Figure 1.3: In a chemical ordering move two atoms are exchanged. A chemical move may not have a great impact on the overall shape of the NP, but the right chemical ordering have a great impact on the energy of the cluster.

In our version of the BH algorithm [38] we use a Monte Carlo–Metropolis acceptance criterion to discriminate whether to accept or refuse a new minimum generated from a move. The new minimum is accepted if a random number extracted between 0 and 1 is lower than:

$$p = e^{\frac{(\tilde{E}_S - \tilde{E}_D)}{k_B T}} \tag{1.2}$$

where $\tilde{E}_S$ is the minimized energy of the starting configuration and $\tilde{E}_D$ is the minimized energy of the new (tentative) configuration generated by the move, k_B is the Boltzmann constant and T is the temperature that acts as a parameter to control how often to accept a move leading to a configuration of higher energy (note that if $\tilde{E}_S - \tilde{E}_D > 0$ then $p > 1$ and the move is always accepted).

When minimizing a complex function, such as the energy of a cluster of atoms, the energy landscape could be extremely complex and present some *funnels*, i.e. portions of the landscape which lead to stable configurations of low energy, in which the algorithm may fall and be trapped, but these configurations are not the best minimum that can be achieved.

In order to address this problem, the BH algorithm can be upgraded by adding to it an on-the-fly structural analysis which may be used to understand which potions of the energy landscape have been explored to try to explore new ones.

The tools for analysing the geometric structures are based on the Common Neighbour Analysis [39, 40], that can classify the local structure depending on its nearest neighbours. The

analysis of the chemical ordering in bi- and multi-component NPs, is made by counting nearest-neighbour bonds of different types, i.e. homo- and hetero-metallic bonds.

The results of the analysis are classified by Order Parameter (OP). The OPs can be calculated at each step or usually only for the accepted steps, depending on the version of the algorithm which is used.

In the following paragraph, we introduce the concept of *Monte Carlo walker in the configurations space* or simply *walker*. The code supports algorithms in which a single walker is used (as in standard BH) and algorithms in which several walkers run in parallel and may also interact with each other.

In the Parallel Excited Walkers algorithm [20] in which the BH algorithm evolves two or more walkers in parallel, the OP are calculated only for the accepted moves. In the PEW algorithm when two walkers falls near each other in the space of the OPs the $\left(\tilde{E}_S - \tilde{E}_D\right)$ from (1.2) changes into $\left(\tilde{E}_S - \tilde{E}_D + E_{exc}\right)$ where E_{exc} increases the probability of accepting a move. An excited walker can escape a funnel occupied by another walker easier than in the case of the standard algorithm thus making it possible to explore a larger variety of regions of the configuration space.

On the other hand, in the HISTO algorithm [21] the OP are calculated at each step because the algorithm decides on whether to accept an attempted move also based on the OP value that would be taken if the move would be accepted. The HISTO algorithm uses the previous history of the simulation to decide whether to accept new moves or not. The information about the previous history is accumulated in a histogram in the OPs space, which contains the frequencies of the different intervals of the OPs that have been visited by the simulation so far. The energy difference for deciding acceptance or rejection is changed from the $\left(\tilde{E}_S - \tilde{E}_D\right)$ of (1.2) to $\left(\tilde{E}_S - \tilde{E}_D + \omega\left(h_S - h_D\right)\right)$ where ω is the parameter that regulates the influence of the histogram and h_S and h_D are the heights of the histogram bars corresponding to the Starting (h_S) and to the Destination (h_D) configurations. The HISTO algorithm favours the possibility of exploring new portions of the OP space.

1.2 PARTICLE SWARM OPTIMIZATION

In their paper, Kennedy and Eberhart [34] described the PSO as a result of their research on social simulation algorithms.

The starting point is to note that the simulation of the flocking of birds can be used not only to try to understand the rules by which bird flocks move around but also to simulate more complex behaviours in society and other contexts. The simplest simulation of bird flocking [41] has three rules that act on the speed of the simulated birds:

- **separation**: steer to avoid crowding local flockmates

- **alignment**: steer towards the average heading of local flockmates

- **cohesion**: steer to move towards the average position (center of mass) of local flockmates

The rule of separation may be dropped if we want to emulate more abstract concept, such as the spreading of ideas in a population because two individuals can share the same thinking. But if we stick only to these rules in a toroidal space[1] we can obtain only a sort of belt made of birds that moves all in the same direction within our simulated space.

To make the *birds* break this behaviour a *craziness* factor can be implemented, that steers randomly an element of the simulation and helps in creating the choreography of the bird flocking with scattering and regrouping. However, this variation of the algorithm is totally artificial. Another thing that helps in improving the realism of the simulation is the matching of the speed between nearest neighbours.

In their article, Heppner and Grenander [42] proposed two methods of making bird go in specific places of the simulated space. "*How do they find food? Anyone who has ever put out a bird feeder knows that within hours a great number of birds will likely find it, even though they had no previous knowledge of its location, appearance, etc.*" [34]. The simplest recipe is adding a *roost* in the space that attracts the flock until the birds land there. Another way is called *Cornfield Vector* and implies that the birds have some memory and share it with the whole flock. At each step of the simulation, the bird will calculate the distance from the cornfield and will remember always the best position visited and share that knowledge with the flock, so that the knowledge of these positions makes each bird steer towards the cornfield by a

---

1 By applying the periodic boundary condition to a rectangular space we obtain the surface of a torus.

random amount[2]. By regulating the steering force, it is possible to vary the result of the simulation from looking realistic, with a low steering force, or by making the flock being rapidly sucked in by the cornfield if the steering force is too high.

Thus Heppner and Grenander [42] noted that they can strip the simulation from the redundant parts, such as the craziness and the simulation would look realistic as well. Moreover, they observed that if the algorithm is also stripped of the nearest neighbours velocity matching reaching the goal would happen faster, tough now the *flock* becomes a *swarm* and the algorithm becomes an optimization algorithm.

Kennedy and Eberhart [34] proposed that the steering force toward the personal and global best position should depend on the distance from those positions:

$$v_x = v_x + rnd * \alpha * (x_{pbest} - x) + rnd * \alpha * (x_{gbest} - x) \quad (1.3)$$

and in particular that α should be 2, in this way at each step half of the birds would *overfly* the target. The momentum has been proven to help in the minimization, so it was kept in the algorithm. All the other characteristics of the flocking simulation were discarded.

1.2.1 *The Particle Swarm Optimization definition*

After taking into account the elements mentioned in the previous section, we note that the PSO algorithm can be reduced to a few statements. At each step of the algorithm each particle

- changes its speed by a random amount towards the best position that the particle itself has visited

- changes its speed by a random amount towards the best position achieved by one member of the swarm

- moves according to its speed

- evaluates its new position in the space accordingly to the function to be optimized

One of the main advantages of the PSO algorithm is that it can be applied to non derivable function because it does not need

---

2 In this case steering means that the speed is changed by a random amount that does not depend on the distance of the bird from the aimed position but only on the relative position (eg.: if $x < x_{best}$ then $v_x = v_x - rnd * \alpha$ else $v_x = v_x + rnd * \alpha$))

the calculation of any gradient. Another advantage is that the algorithm can explore a much bigger portion of the space of the configuration of the optimized function because at each step the function is evaluated in different points.

We tried to apply the PSO to the minimization of NP but with meagre results. In fact, the use of gradients (local minimization) is very effective in the optimization of systems with many degrees of freedom, so that algorithms such as BH have revealed to be more powerful. However, there are other purposes for which the PSO can be effective. As we will see in the following, in looking for the best fit of the Au−S interaction potential, one has to find the global minimum of a function of several parameters. The space of parameters has several dimensions, but much less than the number of degrees of freedom in a nanoparticle. In such relatively small configuration spaces, the PSO becomes quite effective.

2

DENSITY FUNCTIONAL THEORY

Density Functional Theory (DFT) is an *ab–initio* method, in which the electronic structure of a system is calculated by solving Schrödinger's equation for finding the ground state of the electrons in the external field of the nuclei, in the spirit of the Born–Oppenheimer approximation [43]. The PES is then given by the electronic ground–state energy as a function of the set of nuclear coordinates $(\mathbf{R}_1, \mathbf{R}_2, ..., \mathbf{R}_N)$. Even though in principle DFT offers an exact method for calculating the ground–state energy, in practice one is forced to introduce several approximations when dealing with actual problems.

DFT originates from the paper of 1964 by Hohenberg and Kohn [44], who developed a theory that simplified the determination of the ground state of an ensemble of electrons under the action of an external potential. In DFT, instead of concentrating the efforts in the calculation of the wavefunction $\psi(\{\mathbf{r}\})$, which depends on a large number of variables (all coordinates of $m \gg 1$ electrons), one is faced with the problem of determining the electron density $n(\mathbf{r})$, which depends on three spatial coordinates only. The electronic density $n(\mathbf{r})$ is the expectation value of the electron number operator:

$$\mathcal{N} = \sum_{i=1}^{m} \delta(\mathbf{r} - \mathbf{r}_i). \tag{2.1}$$

Let us report some basic results about $n(\mathbf{r})$. Given a normalized state ψ, the expectation value of $\mathcal{N}$ in this state is given by

$$\begin{aligned} n(\mathbf{r}) &= \langle \psi | \mathcal{N} | \psi \rangle \\ &= m \int d\mathbf{r}_2 \cdots d\mathbf{r}_m \psi^*(\mathbf{r}, \mathbf{r}_2, \ldots, \mathbf{r}_m) \psi(\mathbf{r}, \mathbf{r}_2, \ldots, \mathbf{r}_m) \end{aligned} \tag{2.2}$$

To make a practical example let us assume that ψ is expressed by a Slater determinant (we do not consider spin coordinates for simplicity):

$$\psi(\mathbf{r}_1, ..., \mathbf{r}_m) = \sum_P (-1)^P P\{\phi_1^*(r) \phi_2^*(r_2) \cdots \phi_m^*(r_m)\}, \tag{2.3}$$

where the ϕ_i are single–electron wavefunctions, the sum over P indicates the sum over all permutations of electronic variables, and p is the parity of the permutation. In this case, after a few calculations, one obtains

$$(\mathbf{r}) = \sum_{i=1}^{m} |\phi_i(r)|^2.$$
(2.4)

Moreover it is obvious that

$$\int n(\mathbf{r}) \, d\mathbf{r} = m.$$
(2.5)

Let us consider an external potential of the form

$$\sum_i V_{ext}(\mathbf{r}_i).$$
(2.6)

The external potential will be that of the fixed nuclei (or of the ionic cores) in the following. It turns out that the contribution of the external potential can be written in terms of $n(\mathbf{r})$ [43]

$$\langle \psi | \sum_i V_{ext}(\mathbf{r}_i) | \psi \rangle = \int d\mathbf{r} V_{ext}(\mathbf{r}) \, n(\mathbf{r})$$
(2.7)

If the electronic Hamiltonian is written as $H_{el} = T + V_{ee} + V_{ext}$, where T is the kinetic energy and V_{ee} is the Coulomb repulsion between electrons, this result brings us to:

$$\langle \psi | H_{el} | \psi \rangle =$$

$$\left\langle \psi \left| -\frac{1}{2} \sum_i \nabla_i^2 + \frac{1}{2} \sum_{i \neq j} \frac{1}{|r_i - r_j|} \right| \psi \right\rangle + \int d\mathbf{r} V_{ext}(\mathbf{r}) \, n(\mathbf{r}) \quad (2.8)$$

In this equation we have put the electron mass m_e, the (absolute) electron charge e and $\hbar$ all equal to one.

2.1   HOHENBERG AND KOHN THEOREMS

Here below we report the fundamental theorems of DFT, due to Hohenberg and Kohn (HK). We sketch the derivation following the book by R. M. Martin [43]. For a more rigorous and complete treatment, one may refer to the book by Engel and Dreizler [45]. HK theorems read

THEOREM I: For any system of interacting particles in an external potential $V_{ext}(\mathbf{r})$, the potential $V_{ext}(\mathbf{r})$ is determined uniquely, except for a constant, by the ground state particle density $n_0(\mathbf{r})$.

COROLLARY I: Since the Hamiltonian is thus fully determined, except for a constant shift of the energy, it follows that the many-body wavefunctions for all states (ground and excited) are determined. Therefore all properties of the system are completely determined given only the ground state density $n_0(\mathbf{r})$.

THEOREM II: A universal functional for the energy $E[n]$ in terms of the density $n(\mathbf{r})$ can be defined, valid for any external potential $V_{ext}(\mathbf{r})$. For any particular $V_{ext}(\mathbf{r})$, the exact ground state energy of the system is the global minimum value of this functional, and the density $n(\mathbf{r})$ that minimizes the functional is the exact ground state density $n_0(\mathbf{r})$.

The proofs of HK theorems are unexpectedly simple.

Let us start from the first theorem, using the expressions (2.2) for the density and (2.8) for the energy. Let us assume that there exist two external potentials $V_{ext}(\mathbf{r})$ and $V'_{ext}(\mathbf{r})$ which differ by more than a constant and which bring to the same ground state density $n(\mathbf{r})$. So we have two different Hamiltonians H and H' and each one leads to a different ground state ψ and ψ'. But our hypothesis is that ψ and ψ' lead to the same ground state density $n_0(\mathbf{r})$.

Now we can make some simple calculations: since H has not ψ' as its ground state, we have:

$$E = \langle \psi | H | \psi \rangle < \langle \psi' | H | \psi' \rangle \tag{2.9}$$

Now it is possible to rewrite the last term:

$$\langle \psi' | H | \psi' \rangle = \langle \psi' | H + (H' - H) | \psi' \rangle$$
$$= E' + \int d\mathbf{r} \left[V_{ext}(\mathbf{r}) - V'_{ext}(\mathbf{r}) \right] n_0(\mathbf{r}) \tag{2.10}$$

so that

$$E < E' + \int d\mathbf{r} \left[V_{ext}(\mathbf{r}) - V'_{ext}(\mathbf{r}) \right] n_0(\mathbf{r}) \tag{2.11}$$

By the same reasoning for E' we can easily found that:

$$E' < E + \int d\mathbf{r} \left[V'_{ext}(\mathbf{r}) - V_{ext}(\mathbf{r}) \right] n_0(\mathbf{r}) \tag{2.12}$$

If we sum (2.11) and (2.11) we get the following absurd:

$$E' + E < E + E' \tag{2.13}$$

This is a *reduction ad absurdum*, showing that it is not possible to have two different potentials that bring to the same ground state density.

The corollary is a direct consequence: the Hamiltonian is uniquely determined by the ground state. Then from the Hamiltonian, we can determine any state by solving the corresponding Schrödinger's equation. Among all the solutions we find also the ground state, that is the lowest energy solution. This could seem extremely appealing, but it does not give any recipe to determine $V_{ext}(\mathbf{r})$ from a given $n_0(\mathbf{r})$. Moreover, usually one is interested in the reverse problem, i.e. determining $n_0(\mathbf{r})$ when $V_{ext}(\mathbf{r})$ is known.

Proving the second theorem is also simple. If $n_0(\mathbf{r})$ determines uniquely $V_{ext}(\mathbf{r})$, and so the ground state of the system, the ground state energy can be uniquely determined from a universal functional of the density:

$$E[n(\mathbf{r})] = F[n(\mathbf{r})] + \int d\mathbf{r} V_{ext} n(\mathbf{r}) \qquad (2.14)$$

where

$$F[n(\mathbf{r})] = T[n(\mathbf{r})] + V_{int}[n(\mathbf{r})] \qquad (2.15)$$

includes all kinetic and potential energy terms of the interacting system. All functionals presented in (2.14) and (2.15) are universal: T and V_{int} do not depend on V_{ext} and neither the second term of (2.14), because from theorem I we know that V_{ext} is determined by n_0.

Let us consider now two different densities: n_0 from ψ_0 and n' from ψ'. We know that:

$$E_0 = E[n_0] = \langle \psi_0 | H | \psi_0 \rangle \qquad (2.16)$$

It follows immediately that, if n_0 is the ground state density:

$$E_0 = E[n_0] = \langle \psi_0 | H | \psi_0 \rangle < E[n'x] = \langle \psi' | H | \psi' \rangle = E' \qquad (2.17)$$

Thus the Hohenberg–Kohn functional evaluates the density of the ground state always with lower energy than the density of another state. If the functional F was known, then it would be possible to find the exact ground state density and energy by minimizing the total energy (2.14) of the system by making variations in $n(\mathbf{r})$.

The problem is how to use the results of HK theorems for actual calculations. The idea is to arrive to a system of differential equations that can be solved self–consistently. This can be done by following an *ansatz* proposed by Kohn and Sham [46]. Their idea is that it is possible to substitute the interacting electrons with non–interacting fictitious particles in order to simplify the study of the system. Those fictitious particles feel the influence of and external potential $V_{eff}(\mathbf{r})$.

First of all, we note that the functional derivative of a functional of the form

$$F[n] = \int d\mathbf{r} V(\mathbf{r}) n(\mathbf{r}) \tag{2.18}$$

is:

$$\frac{\delta F[n]}{\delta n(\mathbf{r})} =$$

$$\lim_{\varepsilon \to 0} \frac{1}{\varepsilon} \left(\int d\mathbf{r}' V(\mathbf{r}') \left[n(\mathbf{r}') + \varepsilon \delta(\mathbf{r} - \mathbf{r}') \right] - \int d\mathbf{r}' V(\mathbf{r}') n(\mathbf{r}') \right) =$$

$$= V_{ext}(\mathbf{r}) \tag{2.19}$$

Let us start from a hypothetical system of non interacting electrons under an external potential V_{ext}. For such a system the energy functional reads

$$E[n] = T[n] + \int d\mathbf{r} V_{ext}(\mathbf{r}) n(\mathbf{r}) \tag{2.20}$$

where $T[n]$ is the universal functional representing the kinetic energy of the non interacting electrons. In order to minimize E, with a normalization constraint in n, we calculate:

$$\frac{\delta}{\delta n(\mathbf{r})} \left\{ E[n] - \lambda \left[\int d\mathbf{r} n(\mathbf{r}) - m \right] \right\} = 0 \tag{2.21}$$

that brings to:

$$\frac{\delta T[n]}{\delta n(\mathbf{r})} + V_{ext}(\mathbf{r}) = \lambda \tag{2.22}$$

where λ is a Lagrange multiplier.

We also know that this system of m non–interacting electrons has a ground state that can be written as a Slater determinant of wavefunctions that are determined by solving the Schrödinger's equation:

$$\left[-\frac{1}{2} \nabla^2 + V_{ext}(\mathbf{r}) \right] \phi_k(\mathbf{r}) = \epsilon_k \phi_k(\mathbf{r}) \tag{2.23}$$

whose density will be calculated by

$$n(\mathbf{r}) = \sum_{k=1}^{m} |\phi_k(\mathbf{r})|^2 \tag{2.24}$$

Now let us fall back to the interacting electrons system. Its energy functional will be:

$$E[n] =$$
$$= T[n] + \int d\mathbf{r} V_{ext}(\mathbf{r}) n(\mathbf{r}) + \frac{1}{2} \int d\mathbf{r} \int d\mathbf{r}' \frac{n(\mathbf{r}) n(\mathbf{r}')}{|\mathbf{r} - \mathbf{r}'|} + E_{xc}[n].$$
$$\tag{2.25}$$

Each term of this equation deserves a comment.

- $T[n]$ is the kinetic energy of the non–interacting electrons.

- $\int d\mathbf{r} V_{ext}(\mathbf{r}) n(\mathbf{r})$ is the potential energy due to the ions.

- $\frac{1}{2} \int d\mathbf{r} \int d\mathbf{r}' \frac{n(\mathbf{r}) n(\mathbf{r}')}{|\mathbf{r}-\mathbf{r}'|}$ is the mean field contribution to the interaction energy between electrons, called *Hartree energy*, plus the self-energy contribution[1].

- $E_{xc}[n]$ is the universal exchange-correlation functional, which contains all correlations that are not taken into account in the previous terms. The exact form of the exchange-correlation functional is unknown. However, it may be expected that this contribution is not a very large correction to the previous terms in many cases, so that evaluating it by suitable approximations may give accurate results.

Let us now we take the variation of this energy to the respect of the density we can write:

$$\frac{\delta T[n]}{\delta n(\mathbf{r})} + \frac{\delta E_{xc}[n]}{\delta n(\mathbf{r})} + \int d\mathbf{r}' \frac{n(\mathbf{r}')}{|\mathbf{r} - \mathbf{r}'|} + V_{ext}(\mathbf{r}) = \lambda \tag{2.26}$$

As now no approximations were introduced (but remember that $E_{xc}[n]$ is unknown). The analogue to (2.23) is:

$$\left[-\frac{1}{2}\nabla^2 + V_{eff}(\mathbf{r}) \right] \phi_k(\mathbf{r}) = \epsilon_k \phi_k(\mathbf{r}) \tag{2.27}$$

---

1 The Hartree energy without the self–energy is

$$E^H = \frac{1}{2} \sum_{i \neq j} \int d\mathbf{r} \int d\mathbf{r}' \frac{\phi_i^*(\mathbf{r}) \phi_j^*(\mathbf{r}') \phi_i(\mathbf{r}) \phi_j(\mathbf{r}')}{|\mathbf{r} - \mathbf{r}'|}$$

where

$$V_{eff}(\mathbf{r}) = \frac{\delta E_{xc}[n]}{\delta n(\mathbf{r})} + \int d\mathbf{r}' \frac{n(\mathbf{r}')}{|\mathbf{r} - \mathbf{r}'|} + V_{ext}(\mathbf{r}) \qquad (2.28)$$

In summary, what we have obtained is that the $\phi_k(\mathbf{r})$ are wavefunctions for a fictitious system of non interacting electrons with the very same density of the interacting electrons. This has some consequences. A very important one is that the ϵ_k cannot be interpreted as energies of the electronic states. In fact, if we take (2.27), multiply it for $\phi_k^*(\mathbf{r})$, integrate, and then sum over k:

$$\sum_{k=1}^{m} \epsilon_k = T[n] + \sum_{k=1}^{m} \epsilon_k \int d\mathbf{r}\phi_k^*(\mathbf{r}) V_{eff}(\mathbf{r}) \phi_k(\mathbf{r}) \qquad (2.29)$$

we obtain

$$E[n] =$$

$$\sum_{k=1}^{m} \epsilon_k + E_{xc}[n] - \int d\mathbf{r} V_{xc}[n](\mathbf{r}) n(\mathbf{r}) - \frac{1}{2} \int d\mathbf{r} \int d\mathbf{r}' \frac{n(\mathbf{r}) n(\mathbf{r}')}{|\mathbf{r} - \mathbf{r}'|}.$$

$$(2.30)$$

where $V_{xc}[n](\mathbf{r}) = \frac{\delta E_{xc}[n]}{\delta n(\mathbf{r})}$. This notation $V_{xc}[n](\mathbf{r})$ means that V_{xc} is a functional of n and its value is a function of $\mathbf{r}$.

Since V_{eff} contains n, which is expressed in terms of the unknown ϕ_k, Kohn–Sham equations (2.27) must be solved self–consistently, by an iterative procedure as that outlined in fig. 2.1.

2.3 APPROXIMATING $E_{xc}[n]$

Thanks to the Kohn–Sham equations we can solve the problem of finding the ground energy of an electronic system in an external potential. But for doing this in practice, we need to give an explicit expression for $E_{xc}[n]$. As noted previously, the exact form of $E_{xc}[n]$ is unknown, so that approximations are necessary. Here we mention two of them, the Local Density Approximation (LDA) and the Generalized–Gradient Approximation (GGA). Both have been widely used in the literature. GGA will be used later in our calculations. The explicit forms of these approximations can be found in the literature [43, 46–51] Here we briefly summarize their main features.

LDA was proposed already in the original work of Kohn and Sham [46]. They proposed to use the same *jellium* approximation

```
        ┌─────────────────┐
        │  Initial guess  │
        └─────────────────┘
                 │
                 ▼
  ┌──▶┌──────────────────────────┐
  │   │ Calculate effective potential │
  │   └──────────────────────────┘
  │              │
  │              ▼
  │   ┌──────────────────────────┐
  │   │  Solve Kohn Sham equations │
  │   └──────────────────────────┘
  │              │
  │              ▼
  │   ┌──────────────────────────┐
  │   │  Calculate electron density │
  │   └──────────────────────────┘
  │              │
  │              ▼
  │         ◇ self-consistent? ◇
  │   no   ╱                    ╲
  └───────                       
                 │ yes
                 ▼
        ┌──────────────────┐
        │ Output quantities │
        └──────────────────┘
```
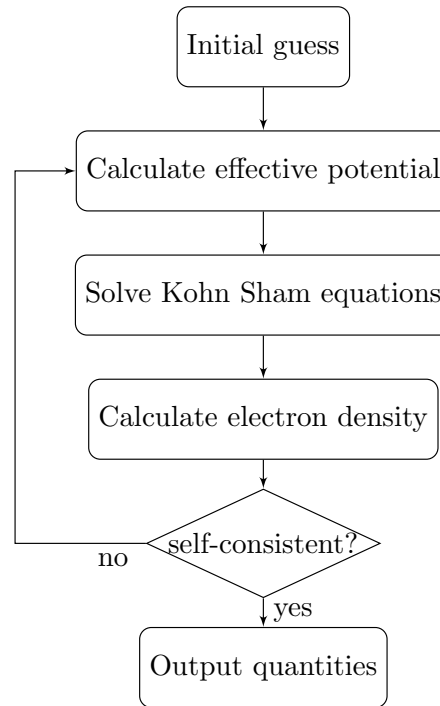
Figure 2.1: The self consistent work flow for solving the Kohn–Sham equations

that often is used for bulk metals. Jellium is a system in which electrons are uniformly distributed in space, together with a uniform background of electronic charge to ensure neutrality. The idea is to calculate the form of the exchange–correlation functional of the jellium model and to use it in the Kohn–Sham equations for real systems. This amounts to assuming that for a real non–uniform system, $E_{xc}[n]$ has locally the same expression as for a jellium of density $n(\mathbf{r})$. LDA is expected to be accurate in systems where gradients of the density are not too large. This is very often the case for infinite metals, but it is more problematic when dealing with finite systems or in general with interfaces, which present interfaces with vacuum where electron density varies rather abruptly. For many metals, and specifically for Ag and Au, LDA overestimates the binding energy between atoms, giving cohesive energies larger than the experimental values.

GGA incorporates corrections which depend not only on the local value of the density but also on its gradient. This makes GGA usually more accurate for finite systems and interfaces. At variance with LDA, GGA tends to underestimate binding in several cases. For Ag and Au, GGA underestimates the cohesive energy. There are several versions of GGA [47–51], corresponding to different approximations. In the following, we will use the

Perdew–Burke–Ernzerhof (PBE) version [51], which is now very widely used and it is considered a reference point for tests.

To compare LDA and DFT–PBE for Ag and Au bulk crystals, in Table 2.1 we report the values of the calculated and experimental cohesive energies, showing that LDA is overbinding and GGA–PBE is underbinding.

	Ag	Au	Pt
LDA	3.61[b]	4.36[b]	6.08[d]
GGA-PBE	2.49[a] - 2.51[b]	2.99[a]-3.04[b]	5.50[a]
Experiment	2.95[c]	3.81[c]	5.84[c]

Table 2.1: Cohesive energies (in eV/atom) of Ag and Au bulk crystals according to LDA and GGA–PBE, compared to experimental values. [a]From Ref. [52] [b]From Ref. [53]. [c]From Ref. [54]. [d]From Ref. [55].

2.4 PSEUDOPOTENTIALS

In the 1934 Hellman [56] proposed an approximation for simplifying the solution of the Schrödinger's equation for the electrons. This approximation consists in solving the Schrödinger's equation only for the valence electrons and consider the core electrons as a perturbation in the potential energy. This drastically reduces the number of electrons to be taken explicitly into account, allowing thus much faster calculations.

Indeed, an all–electron treatment in metallic systems would not be feasible in a practice timescale for this Thesis due to the number of electrons that each metallic atoms would bring to the calculation.

Hellman proposed to treat core atoms by the semiclassical Thomas–Fermi model [57, 58], and to solve the Schrödinger's equation for the valence electrons by using an additional the term as a correction to the potential energy (*the pseudopotential*). This term is:

$$\frac{\partial t_{int}}{\partial n_{int}} \tag{2.31}$$

where t_{int} is the kinetic energy per unit volume and n_{int} the density of the internal electrons.

In more recent times much more sophisticated pseudopotentials for the electrons have been developed. They are classified

according to the type of GGA approximation that they follow, according to the number of electrons which have to be taken into account explicitly (a pseudopotential is more *soft* the less explicit electrons it assumes), and according to the technique used to solve the Schrödinger's equation. Moreover, some pseudopotentials are addressed as *norm–conserving* if they are made with the imposition that the norm of the pseudo–wavefunction is the norm of the true wavefunction [59] after a certain distance R_c from the nucleus. We will give reference in the following to the specific pseudopotentials that we will use in our calculations.

An alternative way to the pseudopotentials is to follow the Projector Augmented Wave (PAW) method [60] proposed by Blöchl. The PAW method, unlike other pseudopotentials, derives its pseudowave–functions using the unmodified all–electron potential and so obtains similar results to an all–electron with frozen core calculation. It is possible to derive a pseudofunction from the PAW method compatible with a plane–wave code that supports the ultrasoft pseudopotential formalism [61].

CLASSICAL POTENTIALS

3.1 THE SECOND MOMENT APPROXIMATION TO THE THIGH BINDING

The Second–Moment Approximation to the Tight–Binding (SMATB), also known as Gupta potential [32] or Rosato-Guillopè-Legrand (RGL) [62] potential, was first derived by Cyrot-Lackmann and Ducastelle [63]. Here below we follow the derivation contained in the book by Spanjaard and Desjonqueres [64].

The purpose of this section is to arrive to a definition of the potential energy surface (PES) according to an atomistic scheme, i.e. to derive an approximate expression for the potential energy E of an aggregate of N metal atoms as a function of their coordinates (which are the coordinates of their ionic cores):

$$E = E(\mathbf{R}_1, \mathbf{R}_2, ..., \mathbf{R}_N). \tag{3.1}$$

Since $E = 0$ for infinite separation between atoms, E coincides with the binding energy of the aggregate. Once the PES is established, the explicit analytical expression for the forces on each atom can be obtained from the gradient of the PES.

3.1.1 *Tight–Binding — General Formulation*

The tight–binding (TB) approximation is derived by solving the Schrödinger's equation for $|n\rangle$:

$$H |n\rangle = E_n |n\rangle, \tag{3.2}$$

using as a base the atomic orbitals:

$$|n\rangle = \sum_{i\lambda} c_{i\lambda} (E_n) |i\lambda\rangle, \tag{3.3}$$

Where H is the one-electron Hamiltonian:

$$H = T + \sum_{i=1}^{N} V_i (\mathbf{r} - \mathbf{R}_i) = T + \sum_{i=1}^{N} V_i \tag{3.4}$$

And the atomic orbitals $|i\lambda\rangle$ are the solutions to the Schrödinger's equation of an isolated atom:

$$(T + V_i) |i\lambda\rangle = E_0^{i\lambda} |i\lambda\rangle, \tag{3.5}$$

T is the kinetic energy operator of the electron and V_i is the atomic potential centered on site i, at position $\mathbf{R}_i$, $|i\lambda\rangle = \varphi_{i\lambda}\left(\mathbf{r} - \mathbf{R}_i\right)$ the atomic orbital centered on site i, with λ labelling the various atomic orbitals on the same site.

By assuming that the atomic orbitals form an orthonormal basis ($\langle i\lambda|j\mu\rangle = \delta_{ij}\delta_{\lambda\mu}$) the TB approximation is derived by calculating the matrix elements in this basis set:

$$H_{ij}^{\lambda\mu} = E_0^{i\lambda}\delta_{ij}\delta_{\lambda\mu} + \langle i\lambda|\sum_{k\neq j} V_k |j\mu\rangle. \qquad (3.6)$$

From the $\langle i\lambda|\sum_{k\neq j} V_k |j\mu\rangle$ (3.6) we can neglect the three–center integrals and the two–center that are not on the first shell of neighbours for the ith atom, due to the rapid decrease of the wave functions. Now we can divide the elements of the matrix into two different groups: the intra–atomic element and the inter–atomic ones, that often are referred to as hopping integrals. The intra–atomic elements are:

$$H_{ii}^{\lambda\mu} = E_0^{i\lambda}\delta_{\lambda\mu} + \langle i\lambda|\sum_{k\neq i} V_k |i\mu\rangle \qquad (3.7)$$

and the hopping integrals are:

$$H_{ij}^{\lambda\mu} = \langle i\lambda| V_i |j\mu\rangle = \beta_{\lambda\mu}^{ij}\left(\mathbf{R}_{ij}\right) \qquad i \neq j. \qquad (3.8)$$

The hopping integrals are responsible of broadening of discrete atomic levels into an energy band, whereas the intra–atomic integrals contribute a shift of the band. $\beta_{\lambda\mu}^{ij}\left(\mathbf{R}_{ij}\right)$ are functions of $\mathbf{R}_{ij} = \mathbf{R}_j - \mathbf{R}_i$ and have been tabulated by the distance and the direction cosines l, m, n of $\mathbf{R}_{ij}$ with a limited number of parameters by Slater and Koster [65].

Now we substitute (3.3) into the Schrödinger's equation and we take into account the various matrix elements, neglecting the shift integrals:

$$\left(E_0^{i\lambda} - E\right) c_{i\lambda} + \sum_{j\neq i}\sum_{\mu} \beta_{\lambda\mu}^{ij}\left(\mathbf{R}_{ij}\right) c_{j\mu} = 0 \qquad (3.9)$$

By solving this equation we can determine the energies of the electrons. If the system is a perfect and infinite crystal with a single atom per unit cell the Bloch theorem can be applied transforming the system from $lN \times lN$ to $l \times l$ (or $N_c l \times N_c l$ where there are N_c atoms in the unit cell).

3.1.2 *The binding energy of transition metals*

Here we sketch the derivation of an approximate expression for the binding energy per atom of a transition metal as a function of the distance between atoms. The derivation follows again the book of Spanjaard and Desjonqueres [64], to which the reader should refer for further details. The metal is here assumed to be made of a single type of atoms. We assume that the binding energy E is the sum of two terms, an attractive (negative) term E_b due to the d–band electrons, and a repulsive (positive) term E_{rep} due to the superposition of core electrons:

$$E = E_b + E_{rep} \tag{3.10}$$

The repulsive term is dominant at small separation R between atoms, while the attractive term is dominant for larger distances. Both terms tend rapidly to 0 for $R \to \infty$.

Let us calculate now the d–band contribution to the energy of the metal. The d band can accommodate up to 10 electrons per atom, so that the number of d electrons per atom N_d is $N_d \leqslant 10$. We assume that, in the isolated atoms, the electrons of level nd, where $n = 3, 4, 5$ for the three transition series, have energy $E_0 = 0$. Now we approach the atoms to each other. The d orbitals superimpose so that a band forms. The band is assumed to be still centered in E_0 (this amounts to neglecting the shift integrals). According to these approximations, the binding energy per atom is given by

$$E_b = 10 \int_{-\infty}^{E_F} En\left(E\right) dE \tag{3.11}$$

where $n(E)$ is the density of states per atom (normalized to one)

$$\int_{-\infty}^{\infty} n(E)dE = 1. \tag{3.12}$$

E_F is the Fermi energy which obeys the equation

$$N_d = 10 \int_{-\infty}^{E_f} n\left(E\right) dE \tag{3.13}$$

The behaviour of E_b does not heavily depend on the form of $n\left(E\right)$, so we can approximate $n\left(E\right)$ with $\tilde{n}\left(E\right)$, which is a rectangular function of width W that must have the same second moment of $n\left(E\right)$:

$$\tilde{n}\left(E\right) = \begin{cases} 1/W & -\frac{W}{2} \leqslant E \leqslant \frac{W}{2} \\ 0 & \text{otherwise.} \end{cases} \tag{3.14}$$

The second moment of $\tilde{n}(E)$ is

$$\mu_2 = \frac{1}{W} \int_{-\frac{W}{2}}^{\frac{W}{2}} E\, dE = \frac{W^2}{12} \tag{3.15}$$

On the other hand, a general expression for the moments of the density of states can be given in terms of the hopping integrals by means of a continued–fraction expansion [64]. The expression for the second moment of the density of states of atom i is

$$\mu_{2i}^c = \frac{1}{5} \sum_{\lambda,\mu=1}^{5} \sum_{j\neq i} \langle i\lambda|H|j\mu\rangle \langle j\mu|H|i\lambda\rangle = \frac{1}{5} \sum_{j\neq i} \mathrm{Tr}\left\{\beta^2(\mathbf{R}_{i}j)\right\} \tag{3.16}$$

where $\beta^2(\mathbf{R}_{ij})$ is the hopping integral matrix from (3.9). The latter expression can be approximated as

$$\mu_{2i}^c = \frac{1}{5} \sum_{n}^{\text{I.N.}} Z_{in}\left(dd\sigma_n^2 + 2dd\pi_n^2 + 2dd\delta_n^2\right) = \sum_{n}^{\text{I.N.}} Z_{in}\beta_n^2 \tag{3.17}$$

where "I.N." stands for "Interacting Neighbours", n is the order of the shell of neighbours, Z_{in} is the number of electrons of the atom labeled i in the n-th shell of neighbours $dd\sigma_n$, $dd\pi_n$, $dd\delta_n$ are the Slater–Koster tabulated hopping integrals and β_n the mean of the hopping integrals. If the crystal is face centered cubic (fcc) or hexagonal close–packed (hcp) $n = 1$ and $\mu_{21} \propto Z_{in}$, otherwise if is body centered cubic (bcc) $n = 1, 2$. Let us take only the first neighbour shell:

$$\mu_{21} = Z_{1n}\beta_n^2(\mathbf{R}) \rightarrow W_{1i}(\mathbf{R}) = 2\sqrt{3Z_{1i}}\,|\beta_1(\mathbf{R})| \tag{3.18}$$

but, since $\mu_2 = \frac{W^2}{12}$

$$W(\mathbf{R}) = 2\sqrt{3\sum_i \mu_{1i}} = 2\sqrt{3\sum_i Z_{1i}\beta_{1i}^2(\mathbf{R})} \tag{3.19}$$

We want to express E_b in terms of μ_2. From (3.13) and (3.14) we calculate E_F as:

$$E_F = \frac{W(\mathbf{R})}{10}(N_d - 10) \tag{3.20}$$

then we can calculate (3.11):

$$E_b = 10 \int_{-\infty}^{E_F} E n(E)\, dE = \frac{W(\mathbf{R})}{20} N_d(N_d - 10) \tag{3.21}$$

and finally

$$E_b = \sqrt{\sum_{f.n.} 3\left(\frac{N_d\,(N_d - 10)}{10}\right)^2 N_d \beta^2\,(\mathbf{R})} = \sqrt{\sum_{f.n.} \Xi^2\,(\mathbf{R})} \quad (3.22)$$

where Ξ is introduced in place of the function that it is used to model the hopping integrals times the various scale factors. In the original work of Slater and Koster this function is a R^{-4} or R^{-5}, but it has been suggested that an exponential form should handle better deformation and stresses [66]. Considering an atom i, the attractive part of its binding energy will depend on the distances $R_{ij} = |\mathbf{R}_i - \mathbf{R}_j|$ between the atoms and other atoms j in the different shells of neighbours:

$$E_{i,b} = -\sqrt{\sum_{j,R_{ij}\leqslant R_c} \Xi\,(R_{ij})} = -\sqrt{\sum_{j,R_{ij}\leqslant R_c} \xi^2 e^{-2q\left(\frac{R_{ij}}{R_0} - 1\right)}} \quad (3.23)$$

where R_c is a cutoff radius which selects which shells of neighbours have to be considered. This expression contains also other parameters (ξ, q, R_0), whose meaning will be explained later in section 3.2. We note that the square root makes $E_{i,b}$ a many–body contribution to the energy. This means that it cannot be expressed as a sum of two–body terms (i.e. of pair contributions).

The repulsive term is usually treated in a phenomenological way. Here, it is assumed to be in the form of the Born–Mayer ion–ion repulsion [63]:

$$E_{i,rep} = \sum_{j,R_{ij}\leqslant R_c} A e^{-p\left(\frac{R_{ij}}{R_0} - 1\right)}, \quad (3.24)$$

where the meaning of the further parameters A, p will be explained in section 3.2.

3.2 THE SMATB POTENTIAL

Now we are in the position of writing explicitly the formula for $E(\mathbf{R}_1, \mathbf{R}_2, ..., \mathbf{R}_N)$. For an aggregate of N atoms of the same type we have [32, 62, 63]

$$E = \sum_{i=1}^{N} E_i, \quad (3.25)$$

with

$$E_i = \sum_{i=1}^{N} (E_{i,rep} + E_{i,b})$$

$$= \sum_{j,R_{ij} \leqslant R_c} A e^{-p\left(\frac{R_{ij}}{R_0}-1\right)} - \sqrt{\sum_{j,R_{ij} \leqslant R_c} \xi^2 e^{-2q\left(\frac{R_{ij}}{R_0}-1\right)}}.$$

(3.26)

E depends on a set of parameters: p, q, A, ξ, R_0. These parameters are usually determined by fitting some experimental properties of the bulk crystal: R_0 is taken as the equilibrium nearest–neighbour separation in the bulk crystal at zero temperature, whereas p, q, A, ξ are fitted to reproduce the cohesive energy, the bulk modulus and some elastic constants [62, 66], or surface energies.

This formula can be generalized to binary systems. In this case, there will be different interaction parameters for the different pairs:

$$\sum_{j,R_{ij} \leqslant R_{c,ab}} A_{ab} e^{-p_{ab}\left(\frac{R_{ij}}{R_{0,ab}}-1\right)} - \sqrt{\sum_{j,R_{ij} \leqslant R_{c,ab}} \xi_{ab}^2 e^{-2q_{ab}\left(\frac{R_{ij}}{R_{0,ab}}-1\right)}},$$

(3.27)

where a is the species of atom i and b is the species of atom j.

Introducing a cutoff on the shells of neighbours is very important to speed up calculations, without introducing any sizeable error due to the exponential decay of the interactions. Moreover, the parameters of the model are usually fitted on bulk crystal properties. When modelling a crystal, periodic boundary conditions must be used, and this implies the necessity of a distance cutoff on the potential energy [67]. Therefore, for consistency, the cutoff must be also imposed when the model is used for finite systems. Unfortunately, the cutoff introduces a discontinuity in the potential energy, which causes some artifacts in the forces (and even worse problems in the second derivatives). Therefore it is necessary to introduce a modification of the potential for distances larger than the cutoff distance in order to produce a PES which is continuous with continuous derivative (indeed, with second derivatives well defined, so that one can calculate the Hessian matrix). This is achieved by linking the potential to zero by a suitable polynomial function of fifth order as explained in the next section.

3.3 LINKING THE POTENTIAL TO ZERO

As explained above, in order to implement this potential in an efficient algorithm we need to modify it in a way that can be calculated only for atoms that are not too far one from another. In this way we can avoid losing some time in calculating near–to–zero contributions from distant atoms. The solution that has been adopted consists in cutting off the potential at a chosen distance and link it to zero with a polynomial in order to have a smooth descent that guarantees no discontinuity in the derivatives that will be used.

To link the potential to zero we can rewrite the two exponential of (3.27) in this form: for the repulsive part:

$$
\begin{cases}
A_{ab}e^{-p_{ab}\left(\frac{r_{ij}}{r_{0ab}}-1\right)} & r_{ij} < R_{c,ab} \\
\alpha_3 \Delta_{ij}^3 + \alpha_4 \Delta_{ij}^4 + \alpha_5 \Delta_{ij}^5 & R_{c,ab} < r_{ij} < R_{e,ab} \\
0 & r_{ij} > R_{e,ab}
\end{cases}
\tag{3.28}
$$

where, for brevity $\Delta_{ij} = \left(r_{ij} - R_{e,ab}\right)$ and for the attractive exponential:

$$
\begin{cases}
\xi_{ab}e^{-q_{ab}\left(\frac{r_{ab}}{r_{0ab}}-1\right)} & r_{ij} < R_{c,ab} \\
x_3 \Delta_{ij}^3 + x_4 \Delta_{ij}^4 + x_5 \Delta_{ij}^5 & R_{c,ab} < r_{ij} < R_{e,ab} \\
0 & r_{ij} > R_{e,ab}
\end{cases}
\tag{3.29}
$$

Since the exponential for the repulsive terms and the one for the attractive term are in fact identical apart from the parameters values we will show how to calculate the values for the parameters of the polynomial of the repulsive part.

The polynomial

$$
\alpha_3 \left(r_{ij} - R_{e,ab}\right)^3 + \alpha_4 \left(r_{ij} - R_{e,ab}\right)^4 + \alpha_5 \left(r_{ij} - R_{e,ab}\right)^5
\tag{3.30}
$$

is obviously zero at $R = R_{e,ab}$, and this is true also for its first and second derivative. The coefficients $a_{5,ab}$, $a_{4,ab}$ and $a_{3,ab}$ are chosen in order to match the function value and its first and second derivatives for $R = R_{c,ab}$. This means that we need to solve a small 3×3 linear system. The results are:

$$
\begin{cases}
a_{5,ab} = \nu_{ab}\dfrac{12\kappa_{ab} + 6\zeta_{ab} + \sigma_{ab}}{2\Delta R_{c,ab}^2} \\[2mm]
a_{4,ab} = \nu_{ab}\dfrac{15\kappa_{ab} + 7\zeta_{ab} + \sigma_{ab}}{\Delta R_{c,ab}} \\[2mm]
a_{3,ab} = \nu_{ab}\dfrac{20\kappa_{ab} + 8\zeta_{ab} + \sigma_{ab}}{2}
\end{cases}
\tag{3.31}
$$

where $\Delta R_{c,ab} = R_{e,ab} - R_{c,ab}$, $\nu_{ab} = A_{ab} e^{p_{ab}\left(1 - \frac{R_{c,ab}}{R_{0ab}}\right)}$ and $\kappa_{ab} = -\frac{1}{\Delta R_{c,ab}^3}$, $\zeta_{ab} = \frac{p_{ab}}{R_{0,ab}\Delta R_{c,ab}^2}$, $\sigma_{ab} = -\frac{p_{ab}^2}{R_{0,ab}^2 \Delta R_{c,ab}}$.
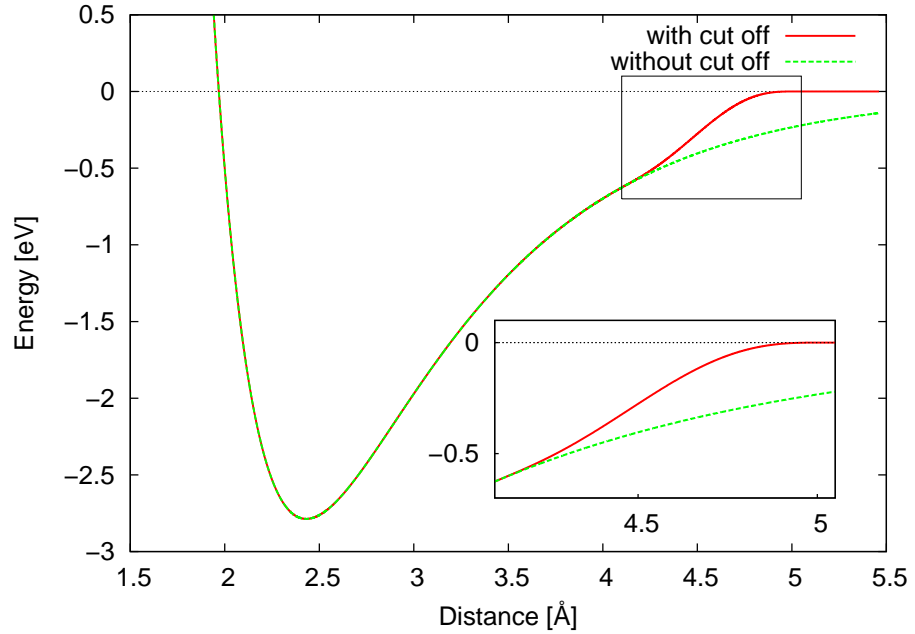

Figure 3.1: The cut off in action for a dimer

For the exponentials in the attractive term we can do the same procedure and obtain the values for the parameters of the polynomial.

The resulting potential for an atomic dimer is shown in fig. 3.1. Typical choices of $R_{c,aa}$ and $R_{c,bb}$ are the second–neighbour distances in the pure a and b crystals, while $R_{e,aa}$ and $R_{e,bb}$ are chosen as the third–neighbour distance [68, 69]. For $R_{c,ab}$ the choice is the second-neighbour distance of the largest atom, and for $R_{e,ab}$ it is the third–neighbour distance of the smaller atom. Since atomic sizes of Ag and Au are almost equal (less than 0.2% difference, see https://www.webelements.com) these distinctions are not really important for this system.

3.4   OPLS

The OPLS [33, 70] force field is one of the most popular atomistic force field for the simulation of polymers, organic solvents, ionic liquids and biological molecules.

The potential energy in OPLS has the form:

$$E\left(\{\mathbf{r}\}\right) = E_{bonds} + E_{angles} + E_{dihedrals} + E_{nonbonded} \qquad (3.32)$$

Where:

$$E_{bonds} = \sum_{bonds} K_r \left(r - r_0\right)^2 \tag{3.33}$$

Is the energy of covalently bonded atoms. It is represented by an harmonic potential that is a good approximation of the bond when atoms are near the equilibrium distance.

$$E_{angles} = \sum_{angles} k_\theta \left(\theta - \theta_0\right)^2 \tag{3.34}$$

Is the energy due to the angles in the molecules, it helps keeping the correct angles in the molecules.

$$\begin{aligned}E_{dihedrals} = \sum_{dihedrals} \Bigg(&\frac{V_1}{2}\left[1 + \cos(\phi - \phi_1)\right] + \frac{V_2}{2}\left[1 - \cos(2\phi - \phi_2)\right] \\ &+ \frac{V_3}{2}\left[1 + \cos(3\phi - \phi_3)\right] + \frac{V_4}{2}\left[1 - \cos(4\phi - \phi_4)\right]\Bigg)\end{aligned} \tag{3.35}$$

The dihedral energy represent the energy due to the torsion of couples of atoms within the molecules.

$$E_{nonbonded} = \sum_{i>j} f_{ij} \left(\frac{A_{ij}}{r_{ij}^{12}} - \frac{C_{ij}}{r_{ij}^{6}} + \frac{q_i q_j e^2}{4\pi\epsilon_0 r_{ij}} \right) \tag{3.36}$$

The non–bonded energy represents the interaction between atoms that belong to different molecules, and between atoms within the same molecule separated by at least three bonds. The contribution of this term to the total energy is due to the electrostatic interaction represented by the Coulomb term and by the long distance interaction represented by the van der Walls term.

Parameters for the simulations are both fitted on experimental data and/or on DFT calculations. The Lennard–Jones (LJ) parameters are derived only for interactions between atoms of the same species. The target properties such as density, crystalline structure, partitioning free energy, etc. are derived by experiments and used as fit target. The LJ parameters for interaction between two different species are derived by applying the geometric mixing rule[1] for both the equilibrium distance an the interaction intensity. All the other parameters, the partial charges and the bonded interactions are derived by using the results of *ab-initio* calculations as target.

---

[1] $A_{ij} = \sqrt{A_{ii}A_{jj}}$
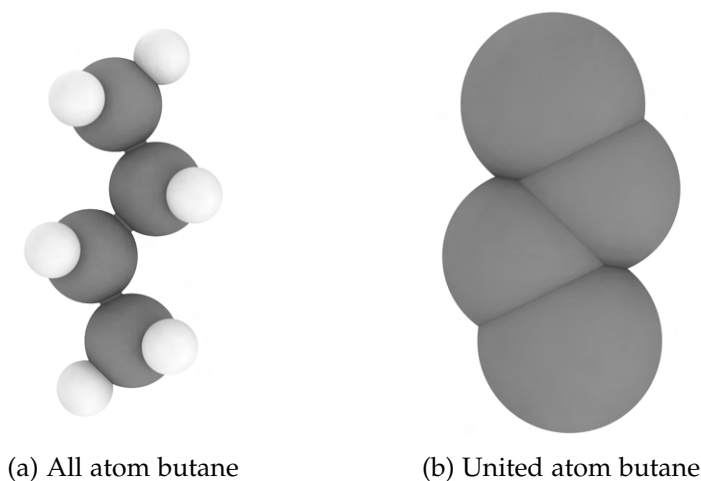
(a) All atom butane

(b) United atom butane

Figure 3.2: This is an example of the difference between an all atom model, in which each atoms is taken into account and an united atom simulation in which the hydrogen atoms are grouped in a bigger bead with the carbon to which they are covalently bonded In these figures the radii of the spheres are in scale to the radii of the models

Before starting an OPLS simulation the user maps the system in order to instruct the program in calculating the right therm of the potential between the right atoms. The "map" of the system instructs the MD program with the specific atoms that forms couples, triplets and quadruplets in their molecules, so that during the simulation the energies and the forces due to E_{bonds}, E_{angles} and $E_{dihedrals}$ are correctly calculated.

OPLS was proposed in 1988 by Jorgensen and Tirado-Rives [33] in a united atom formulation, this means that the hydrogen atoms bounded to the carbon atoms are considered within the carbon atom. Later, in 1996 by Jorgensen, Maxwell, and Tirado-Rives [70], in an variation with all atom considered during the calculations, referred as OPLSAA. In the contest of this work, we intend to use the united atom formulation of OPLS to simulate the organic molecules on the gold NPs.

Part III

RESULTS

NEW GLOBAL OPTIMIZATION ALGORITHMS

4.1 FROM A MONOLITHIC ALGORITHM TO A MODULAR ALGORITHM: BH++

In my Master Thesis, I rewrote the FORTRAN 90 BH code developed by our group some years ago [21] porting it to C++, improving its speed and adding new functionalities, such as an interface with DFT packages. Along with the main objective of my PhD thesis I continued this work and refined the program by adding further functionalities and improving both the user experience and the accessibility to the code.

C++ features give developers more flexibility than FORTRAN in how to organize the code. In particular, I used these features to add layers of modularity both on the development side and on the user experience side.

We call the new program *BH++*.

Global optimization is a quite difficult task. Quite often, even systems that may look similar at a first glance need rather different optimization strategies to achieve good results within a reasonable time. In addition, systems may differ in the number of atoms, in the size of the different atomic species and in their tendency to alloying or to phase separation. The modularity of BH++ gives the users a much larger variety of tools to attack the optimization problem than the previous code.

In BH++, a developer will find easier changing the interaction potential in the algorithm, and also to add new post-processing and analysis modules. And even adding new moves (see section 1.1) is simpler and faster to implement. Also changing how the main BH procedure will act during the optimization is a matter of creating a new file and writing only the parts of the algorithm that will behave differently, eliminating the risk of error due to the copy–paste on large chunks of code.

In BH++ the user will find some new features. When running optimization by using multiple walkers in parallel, the parameters associated to each walker can be chosen independently. This means that each walker has its type of evolution algorithm, its own set of move types, each type being accepted at its tempera-

ture. In addition, BH++ is not limited to binary systems, but it can treat multi-component alloys.

BH++ has been used to prototype new optimization algorithms based on evolutions of the classical BH for optimizing nanoalloys. These new algorithms will be described in the next section, and then tested in a few benchmark examples to test their efficiency.

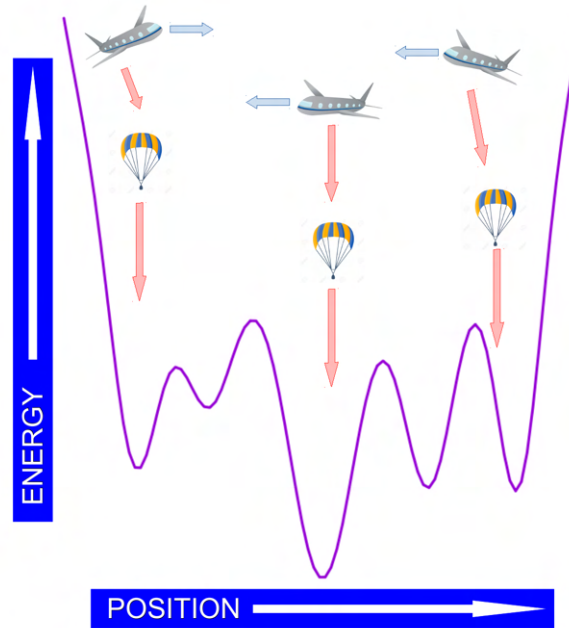## 4.2   A NEW ALGORITHM: FLYING AND LANDING WALKERS

Figure 4.1: Basin Hopping Flying and Landing

We are proposing a new variation of the BH algorithm for the optimization of metallic nanoalloys. We call this new algorithm *Flying and Landing* walkers (F/L algorithm).

This new algorithm aims to efficiently optimize both geometric shape and chemical ordering within the same search. In fact, previous works on the optimization of nanoalloys [38] have shown that the optimization is more efficient if geometric shape and chemical ordering are optimized at the same time. This means that including both shape-changing moves and exchange moves in the same BH search allows a faster convergence to the lowest-energy structures. Moreover, each type of move has to be accepted at its own temperature [38]. Specifically, Brownian and shake moves needs to be accepted at high temperatures

(1500-3000 K for metal nanoparticles) while exchange and bonds moves are better accepted at lower temperatures (100-700 K).

This BH scheme including different types of moves accepted at different temperatures, was favourably tested in the optimization of AuCu and AuRh nanoparticles of size 400 atoms and different compositions [38]. These systems were representative of highly miscible (AuCu) and weakly miscible (AuRh) nanoalloys. Our new F/L algorithm aims at a further efficiency improvement. Here below we describe the F/L algorithm works and test it against the same benchmarks usen ref [38], i.e on AuCu and AuRh nanoparticles of 400 atoms modelled by the Gupta force field.

At variance with standard BH, in which all walkers, albeit different in their moves and temperatures, perform the same task, in F/L there are two types of walkers with quite different tasks.

The first type of walkers is called *Flying* walkers. Flying walkers are set up with a standard evolution algorithm (such as the standard BH or the *parallel excited walker* [20] algorithm). Their moves aim mainly at the optimization of the geometric shape of the NP. These shape-changing moves are associate to very high acceptance temperatures to help the walker to explore a large portion of the configurations space. It may be useful that the Flying walkers make a small percentage of exchange moves and surface rearrangement moves, both accepted at low temperatures, to avoid the generation of very irregular shapes and high-energy chemical ordering patterns.

The second type of walkers is called *Landing* walkers. A Landing walker is associated to each Flying walker. Landing walkers explore the configuration space following the standard BH algorithm. They are armed with a set of moves that is aimed mainly at optimizing the chemical ordering of the NP, with in addition some shape-changing move to cure surface defects. All these moves are accepted at low temperatures to quickly go down in energy.

The key of F/L is the relationship between a Flying walker and its associated Landing walker. Essentially, the Landing walker picks up from time to time configurations found by the Flying walker and use them to go down deep in energy by refining chemical ordering and eliminating surface defects. The rule by which the Landing walker picks up configuration from the Flying walker is explained below.
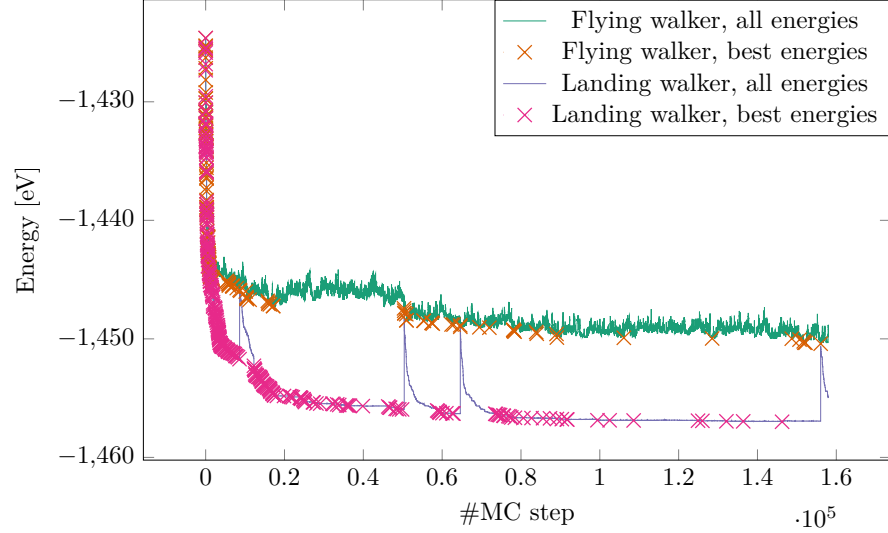
Figure 4.2: Evolution of the energy during optimization of an $Au_{300}Cu_{100}$ nanoparticle. In this simulation, a single Flying walker is used together with its associated Landing walker, which is restarted according to the probability of eq. (4.1) with $\alpha = 1$. When the Landing walker is restarted its energy suddenly increases to match the energy of the Flying walker, and then sharply decreases due to the exchange and surface rearrangement moves accepted at low temperature.

When a Flying walker finds a new individual best minimum (i.e. it finds a new structure whose energy is lower than any structure found by that walker so far) it needs to decide whether to its associated Landing walker has to be *restarted*. By *restart* we mean that the Landing walker picks up the present configuration of the Flying walker, and continues its evolution from that configuration by its own rules. The probability of restarting the Flying walker depends on the energy of the last previous restart and the present energies of the two walkers:

$$p_{restart} = \left| \frac{E_{dive} - E_{new}^{FL}}{E_{dive} - E^{LN}} \right|^{\alpha} \tag{4.1}$$

Where E_{dive} is the energy at the last previous restart, E_{new}^{FL} is the new minimum energy of the Flying walker, E^{LN} is the last accepted energy by the landing walker and $\alpha \in [0, 1]$ is an exponent that regulates the frequency of the restarts of the landing walkers. For $\alpha = 0$ the Landing walker is restarted each time the Flying walker improves its best energy, increasing α make restarts less frequent, which may be beneficial to the optimization efficiency.

Here below we show that this way of separating chemical ordering optimization from shape optimization within the same search run is clearly more efficient than previous approaches in the literature [38] for nanoalloys of considerably large size (see fig. 4.3 and fig. 4.5).

As in Ref. [38], we consider the optimization of AuCu and AuRh nanoalloys of size N = 400, with compositions $Au_{200}Cu_{200}$ and $Au_{200}Cu_{200}$, respectively. AuCu is a strongly intermixing system, while AuRh tends to phase separation. In both cases, the larger atomic size of Au and its lower surface energy are expected to cause some degree of Au surface segregation. Since these systems present quite different tendencies with respect to the intermixing of atomic species, the optimization of chemical ordering is performed by using different types of exchange moves [38]. The lowest-energy structures found for these nanoalloys are shown in figs. 4.4 and 4.6. In both cases, the best structures belong to the icosahedral family, with an extended atomic island partially covering the icosahedron of 309 atoms. On the contrary, optimal chemical ordering is quite different being intermixed with Au surface enrichment for $Au_{200}Cu_{200}$ and Rh@Au core@shell for $Au_{300}Rh_{100}$.

As a benchmark to verify the efficiency of the F/L algorithm, we perform 100 independent simulations of 300000 Monte Carlo steps each for both AuCu and AuRh, and compared them to 100 simulations in which we use the best multi-temperature BH approach that was used in Ref. [38]. In both BH and F/L simulations the same types of moves were used. The results are shown in figs. 4.3 and 4.5, where we plot the histogram of the energies of the best structures found in all simulations, compared to the energy of the global minimum (i.e. the best structure found in all simulations) which is set to zero. It turns out that F/L performs much better than BH. In AuCu, the best structures found by F/L were within 0.5 eV of the global minimum in 27 cases over 100, and the algorithm was able to locate the global minimum. On the other hand, BH was able to terminate within 0.5 eV from the global minimum only in 9 cases over 100, never finding the global minimum but only the third-best isomer. In AuRh, final structures within 0.5 eV from the global minimum were found by 38 and 13 times by F/L and BH, respectively. Both algorithms were able to converge to the global minimum, four times for F/L and two times for BH.
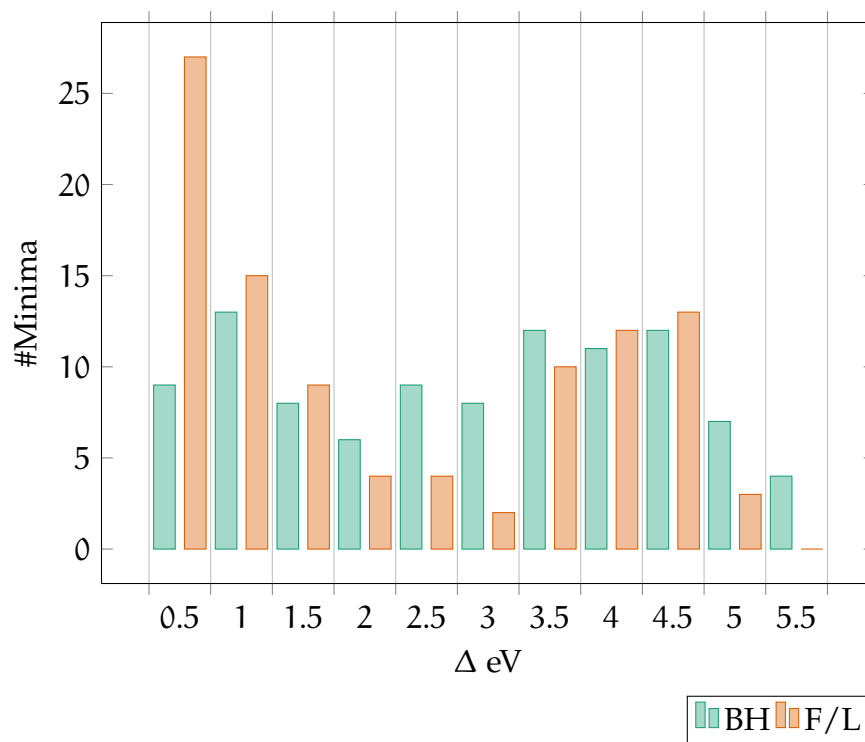
Figure 4.3: These histograms include the result of the minimization of the NP $Au_{200}Cu_{200}$ from the older [38] and the newer F/L algorithms, 100 BH minimizations with 300000 steps were done with each algorithm. The horizontal axis is the distance in energy from the known best minimum. The energies are in eV and the columns have a width of 0.5 eV.
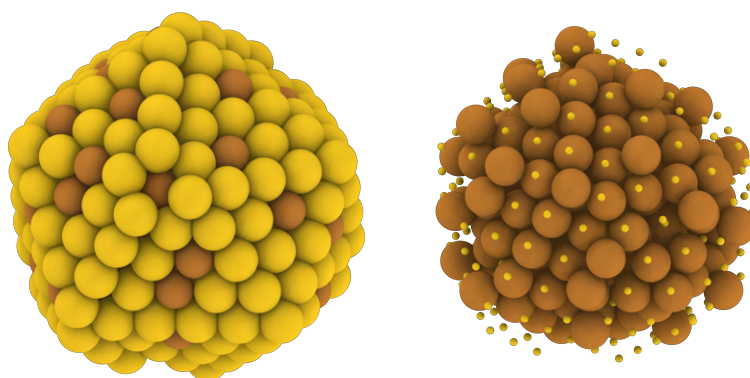

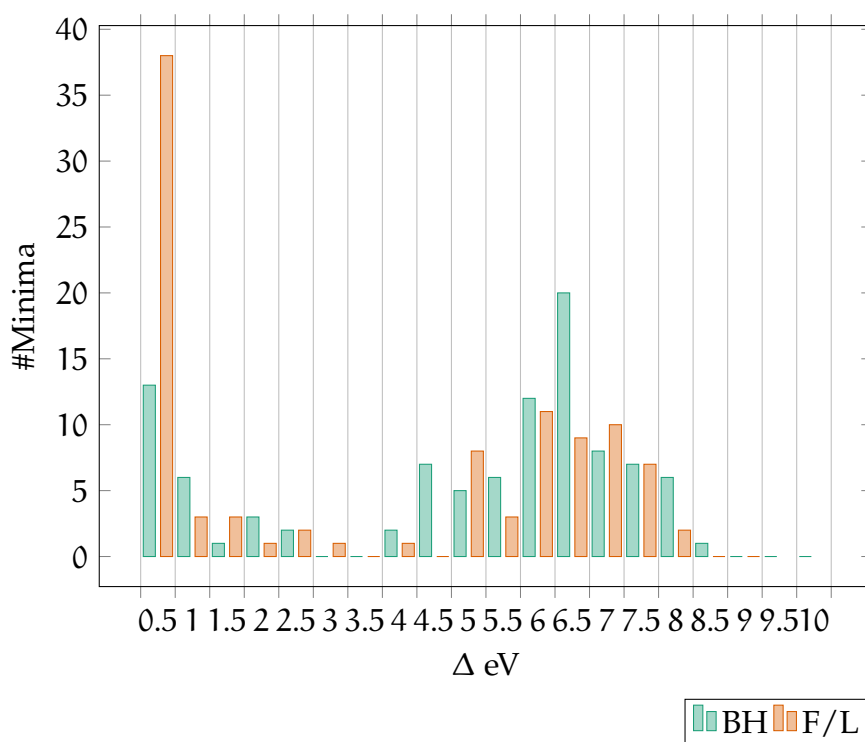Figure 4.4: The best minimum found for $Au_{200}Cu_{200}$. On the right, the gold atoms are rendered as small spheres.

Figure 4.5: These histograms include the result of the minimization of the NP $Au_{300}Rh_{100}$ from the older [38] and the newer F/L algorithms, 100 BH minimizations with 300000 steps were done with each algorithm. The horizontal axis is the distance in energy from the known best minimum. The energies are in eV and the columns have a width of 0.5 eV.
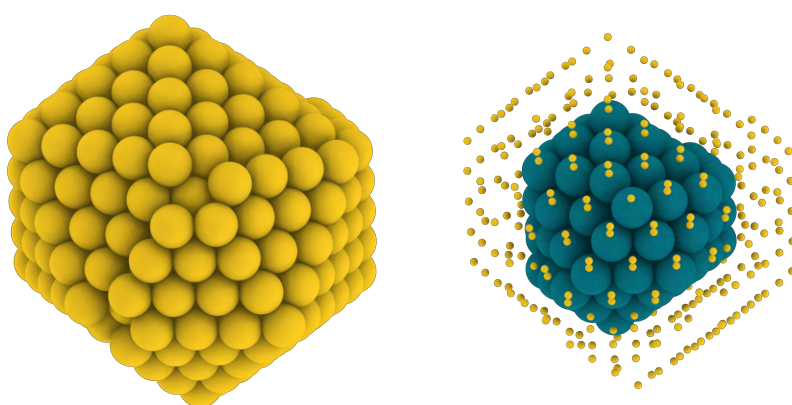

Figure 4.6: The best minimum found for $Au_{300}Rh_{100}$. On the right, the gold atoms are rendered as small spheres.

CHEMICAL ORDERING OPTIMIZATION IN Ag−Pt CLUSTERS

In this chapter, I will expose my contribution to the article in ref [24] (see also the Supplementary Information of the article). This article contains both experimental and simulation results about the equilibrium structures of AgPt nanoalloys. The main result of this paper is the discovery of a new type of nanoparticle structures, presenting the $L1_1$ ordered phase surrounded by an ultrathin Ag shell ($L1_1$@Ag-skin structures, see below). The $L1_1$ phase in a fcc structure is an alternance of close-packed (111) planes of pure Ag and pure Pt atoms. The segregation of the Ag shell is due to the much lower surface energy of Ag with respect to Pt [71]. The $L1_1$@Ag-skin structures are observed only in the extreme nanoscale limit because their stability range is below diameters of 3 nm.

This result is of great interest, because it is a striking counterexample about a trend which is commonly assumed to generally hold for nanoscale systems. In fact, the common wisdom about the stability of ordered phases in NPs is that the stability range of an ordered phase decreases with decreasing size. Well-known examples of this tendency are the decrease of the order-disorder transition temperature in CoPt nanoalloys [72] and the decrease of the melting temperature in Au NPs [73].

The experiments and simulations of AgPt reported in Ref. [24] show that this is not really a general rule, because in AgPt nanoalloys, an increase of the system size can have the opposite effect: for diameters D up to about 2.5 nm, a well-ordered intermetallic phase is found to be stable at equilibrium, but, above this size, either the ordered phase breaks down into multiple, less-ordered domains, or its regular arrangement is interrupted by defects, such as faults in the sequence of Ag and Pt alternating atomic planes. The ordered phase observed at small sizes is characterized by the segregation of a very thin shell at the NP surface. The breaking of this phase in larger NPs is then demonstrated to be caused by stress accumulation in the internal part of the NPs. The accumulation of stress originates from the size mismatch between Ag and Pt atoms.
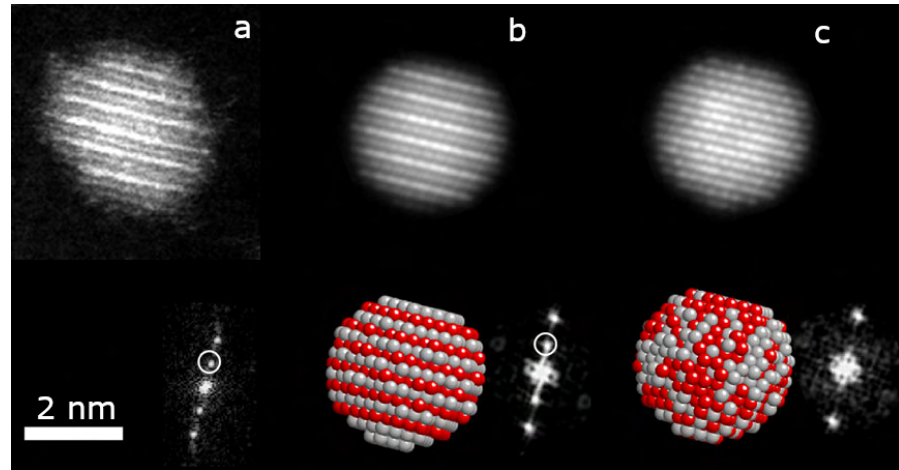
Figure 5.1: In **a**, the NP is a zoomed STEM-HAADF image of a NP presenting a L1$_1$ phase. The **b** and **c** images are two simulates NP, respectively with the L1$_1$ phase and a random arrangement. Under each NP representation there is the result of the fast Fourier transform(FFT) of that image that shows the eventual superstructure within the NP. Figure taken from Ref. [24]

Experimentally, the nanoparticles were grown at room temperature by depositing simultaneously Ag and Pt atoms on an amorphous carbon substrate under ultrahigh vacuum conditions. This deposition procedure produced intermixed metastable structures which were equilibrated by annealing. The main results of this work concern the analysis of the equilibrium AgPt nanoparticles. The experiments were performed in the group of the University of Orléans by Jérome Pirart, Pascal Andreazza and Caroline Andreazza-Vignolle.

The results were interpreted by means of DFT calculations and of Monte Carlo simulations using atomistic force fields. Simulations using force fields were made in the group of CINaM/C-NRS in Marseille, by Alexis Front and Christine Mottet, whereas my contribution was to perform the DFT calculations and global optimization searches.

5.1 EXPERIMENTAL RESULTS

In bulk samples at equilibrium, the phase diagram of AgPt presents an ordered L1$_1$ for a narrow range of compositions around 50%at [74]. AgPt crystallizes in the fcc lattice.

The samples were observed after codepositing Ag and Pt at room temperature on an amorphous carbon grid, annealing at

a temperature of 400 °C, and cooling back to room temperature. Observations by high angle annular dark field in scanning transmission electron microscope (STEM-HAADF) showed that the nanoparticles had an $L1_1$@Ag-skin structure for sizes up to D ∼ 2.5 nm. The $L1_1$@Ag-skin nanoparticles presented an internal $L1_1$ structure encapsulated in an Ag skin, i.e. a very thin Ag shell whose thickness is often of a single atomic layer (monolayer) (fig. 5.2). On the contrary, larger NPs presented much less ordered arrangements, with multiple domains and other defects.
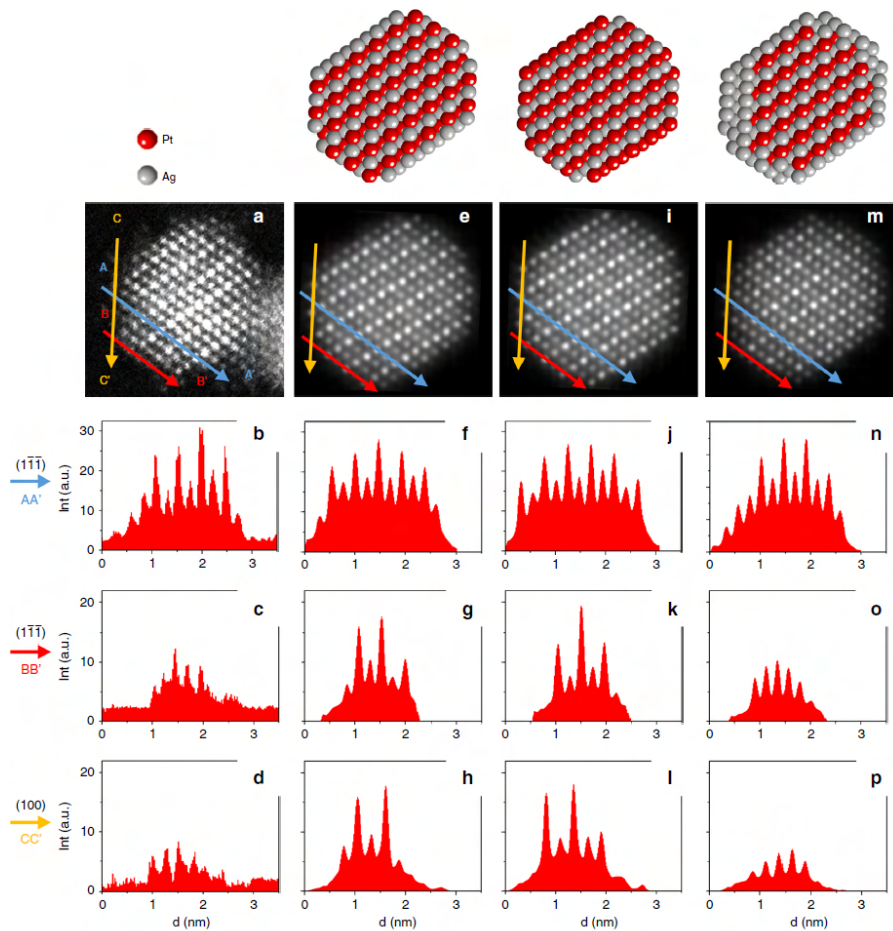

Figure 5.2: A 2.8 nm NP (**a**) experimental STEM–HAADF images and three simulated STEM–HAADF images **e** and **i** in a pure $L1_1$ phase and **m** with the $L1_1$@Ag-skin phase. Below each STEM–HAADF image the graphs show the intensity profiles (AA') and (BB') along the $(1\bar{1}\bar{1})$ plane, and (CC') along the (100) plane. The simulated data that show more similarity with the experimental are the one under the **m** pitcure. Figure taken from Ref. [24]

5.2   DFT CHEMICAL OPTIMIZATION

In support to the experimental result, we contributed by looking for the optimal chemical ordering by means of our BH–DFT interface (see section 4.1). We optimized chemical ordering of small AgPt nanoparticles, whose size (79 atoms) was chosen to allow the $L1_1$@Ag-skin keeping at the same time the computer calculations within a reasonable time. In addition we performed DFT calculations on some further representative configurations.

All the BH runs in this section were done by using only the exchange move, and keeping the cluster structure fixed (apart from local relaxations). Therefore our BH optimized only the chemical ordering of our samples, leaving the geometrical shape almost intact. The BH–DFT algorithm was run by using CP2K [23](cp2k.org) and some calculations were checked by using Quantum ESPRESSO [75](quantum-espresso.org).

The CP2K calculations were done with Fermi–Dirac smearing at 600 K and using the included basis set for Pt (using the basis set DZVP-MOLOPT-SR-GTH-q18 and potential GTH-PBE-q18) and Ag (using the basis set DZVP-MOLOPT-SR-GTH-q11 and potential GTH-PBE-q11).

The Quantum ESPRESSO calculations where done using PBE exchange-correlation (xc-) functional [51, 76] with ultrasoft method type scalar-relativistic pseudopotentials. The energy cutoff for wave functions was 40.0 Ry and the cutoff energy for charge density was 160.0 Ry. Eigenvalues and eigenstates of the Kohn–Sham Hamiltonian have been calculated applying a Marzari-Vanderbilt smearing technique with a broadening of 0.002 Ry.
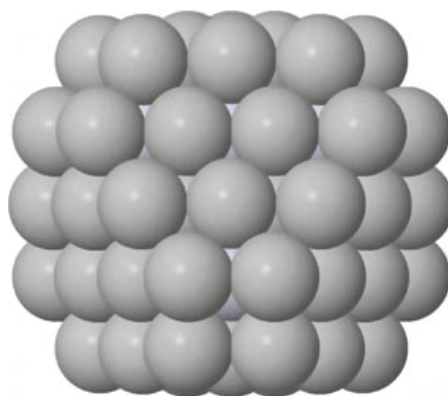

Figure 5.3: A 79 atoms truncated octahedron (TO)

We chose to use a TO of 79 atoms (see fig. 5.3) to simulate the NPs in the experiment. The 79 TO is the smallest NP that

has enough atoms to support an L1$_1$@Ag-skin configuration. In particular, this structure has 60 surface sites, 18 subsurface sites and the central site. The perfect L1$_1$@Ag-skin can be obtained at the composition Ag$_{67}$Pt$_{12}$.

Before running our global optimization searches, we checked for the optimal placement of an isolated Pt impurity, i.e. we considered all possible placement of the Pt atom at composition Ag$_{78}$Pt$_1$ and locally minimized the structures. We found that the most favourable placements of the Pt atom are in subsurface sites over the others. In fact, surface sites and the central site turn out to be quite unfavourable. According to CP2K calculations, Pt atoms will even slightly favour being placed at the centre of a (111) surface facet rather than occupy the central site (see fig. 5.4).
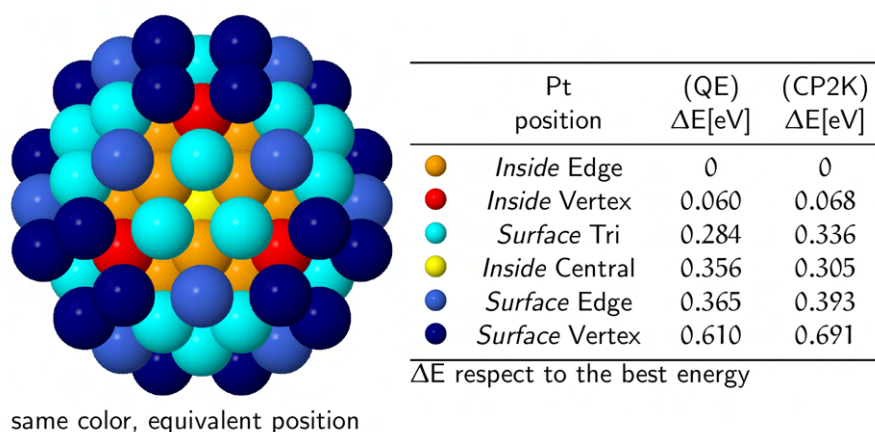

Pt position	(QE) ΔE[eV]	(CP2K) ΔE[eV]
Inside Edge	0	0
Inside Vertex	0.060	0.068
Surface Tri	0.284	0.336
Inside Central	0.356	0.305
Surface Edge	0.365	0.393
Surface Vertex	0.610	0.691

ΔE respect to the best energy

same color, equivalent position

Figure 5.4: The Ag$_{78}$Pt$_1$ TO has six inequivalent position for the Pt impurity. In the table, we indicated the difference in energy from the best site. We used both Quantum ESPRESSO (QE) and CP2K to compute these results. Both codes showed the same behaviour, except that CP2K seems to favour the central position with respect to one of the facet positions. For both cases, the subsurface positions are by far the most favourable. Figure taken from Ref. [24]

On the Ag$_{73}$Pt$_6$ NP we performed DFT calculations to confirm whenever Pt atoms would prefer to occupy the subsurface sites even in presence of other Pt atoms, and which arrangement would be preferred (see fig. 5.5).

From the experimental data, the presence of a Ag skin on the NP was observed. To confirm at the DFT level that the Ag skin will favour the stability of the L1$_1$ phase, we performed BH with only exchange moves on Ag$_{43}$Pt$_{36}$ and Ag$_{36}$Pt$_{43}$. For these
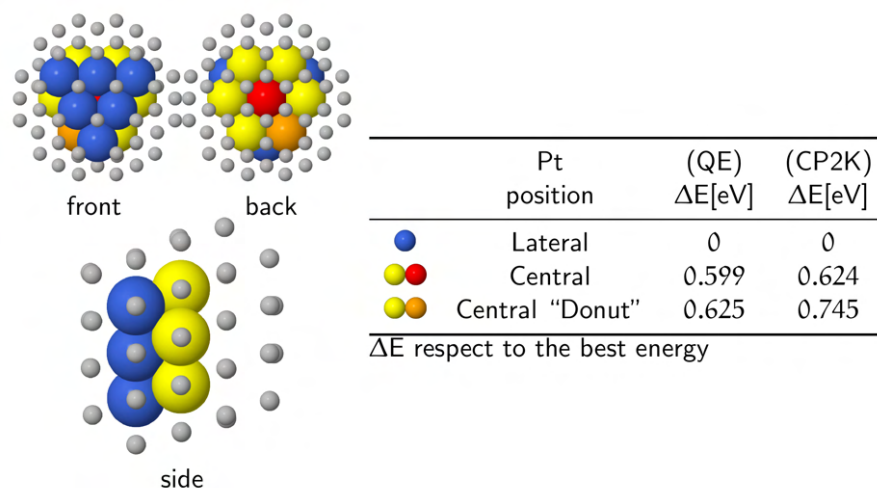
	Pt position	(QE) ΔE[eV]	(CP2K) ΔE[eV]
●	Lateral	0	0
●●	Central	0.599	0.624
●●	Central "Donut"	0.625	0.745

ΔE respect to the best energy

Figure 5.5: We calculated three different configurations of the $Ag_{73}Pt_6$ TO: with the Pt atoms right under the surface or in the centre of the NP. In the table, we indicated the difference in energy from the best configuration. We used both QE and CP2K to compute these results, both code showing the same behaviour. Figure taken from Ref. [24]

compositions, perfect $L1_1$ phases can be built, with Ag and Pt alternating $L1_1$ planes, and without Ag-skin. These structures were used as starting configurations of our global optimization searches of chemical ordering. In a few BH steps, the optimizations strongly changed the chemical ordering by making the Pt atoms to occupy all the internal sites, with the Ag atoms forming an incomplete surface shell. Therefore $L1_1$ phase without Ag-skin was shown to be very unfavourable from an energetic point of view (see fig. 5.6).

Finally, we performed BH runs with only exchange moves on the $Ag_{67}Pt_{12}$ NP, starting both from a completely random configuration and from configurations with only Ag atoms on the surface and all the Pt atoms in the inside. The stoichiometry of this NP was chosen because it can be assembled in a perfect 79 atoms TO with the $L1_1$@Ag-skin structure, as stated above. Our optimizations brought us to best configurations nearly equivalent to the $L1_1$@Ag-skin, the best obtained configuration with our codes is indistinguishable in energy from the $L1_1$@Ag-skin, but present a Pt atom in the skin substrate that connects the two internal Pt planes.

In summary, our DFT results confirmed that $L1_1$@Ag-skin structures are energetically favourable, in very good agreement with the experiments. Monte Carlo simulations using atom-

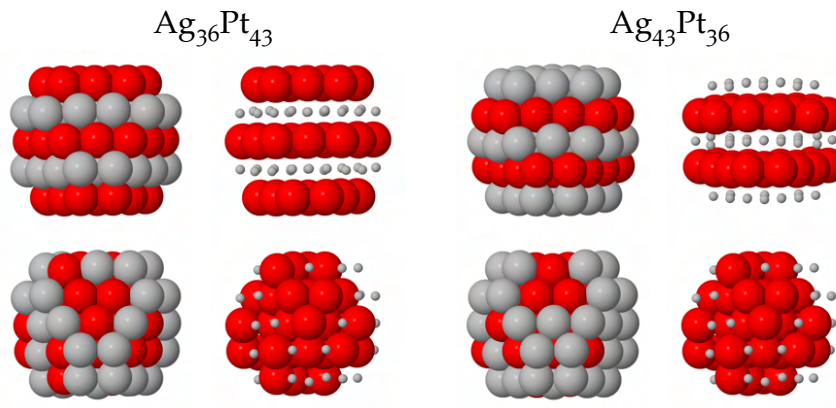$Ag_{36}Pt_{43}$ $Ag_{43}Pt_{36}$

Figure 5.6: The unprotected $L1_1$ are not stable. On the first row, we can see the starting position of the BH, with the pure $L1_1$ phase. On the bottom best energy configuration found by the BH procedure for the initial configuration above. For each configuration, we added a representation with the silver atoms reduced in size. The Pt atom are in red, the Ag atoms are in grey. Figure taken and adapted from Ref. [24]

istic force fields were then done to study the behaviour of the $L1_1$@Ag-skin structures for larger sizes and at finite temperature. These simulations showed that the $L1_1$@Ag-skin structure is indeed favourable up to sizes of about 2.5 nm, corresponding to a few hundred atoms, and then it breaks due to the development of internal stress in the nanoparticles. These results were also in very good agreement with the experiments.
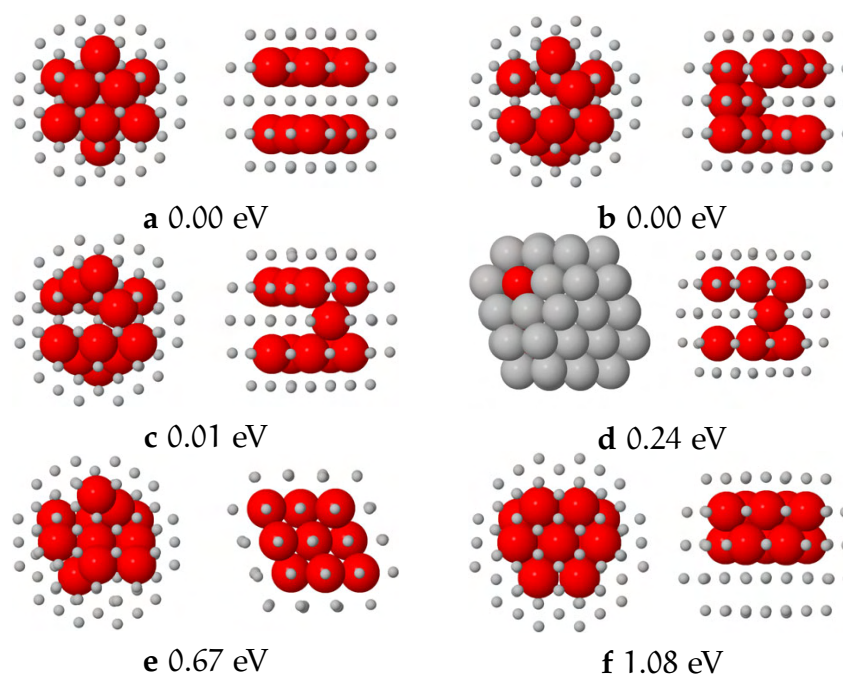
a 0.00 eV   **b** 0.00 eV

c 0.01 eV   **d** 0.24 eV

e 0.67 eV   **f** 1.08 eV

Figure 5.7: The BH results on the $Ag_{67}Pt_{12}$: we listed the energy differ-
ence from the best configurations. For each configuration,
we listed two different views, the Pt atoms are in red, Ag
atoms are in grey and smaller to give a better view of the
internal configuration, except for the configuration **d**, to
show the single platinum on the NP skin. The configura-
tion **f** with the two Pt planes touching is very unfavourite.
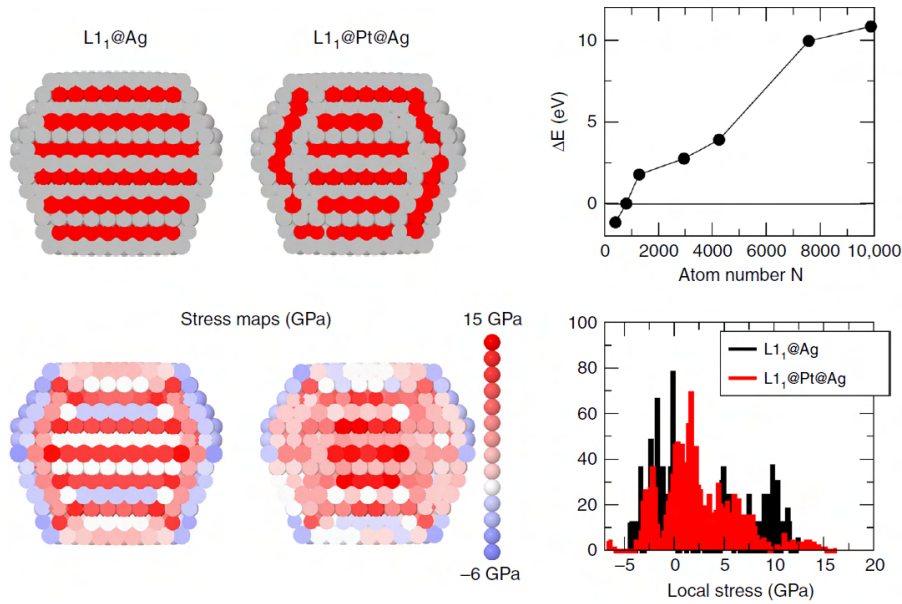Figure taken and adapted from Ref. [24]

Figure 5.8: The stress maps on the left show the results of classical calculation for L1$_1$@Ag core/shell and L1$_1$@Pt@Ag core/subshell/shell in TO of 1289 atoms. On the right, the top graph illustrates the energy difference between the L1$_1$@Ag and L1$_1$@Pt@Ag configurations, when the sign is positive the latter is the stable configuration. On the bottom right the graph shows the stress distribution for the TO with 1289 atoms.

6

DEVELOPMENT OF AN Au−S INTERACTION POTENTIAL

As mentioned in the Introduction, the biomedical applications of metal NPs often require the NP to be functionalized by organic molecules [77]. The NP organic shell can be covalently or non–covalently bound to the NP [78]; it can provide solubility [27], biocompatibility [26], target selectivity to the NP; in most advanced applications, it can store the drug [6, 7] and control its release under a appropriate external stimuli [28].

Gold NPs, in particular, are promising drug vectors and imaging nanoagents, due to their compatibility and optical properties [11, 12]. Most often they are functionalized by thiolated molecules, that is, molecules that bind to the gold surface via Au−S bonds. Thiolated flat Au surfaces, thiolated nanoparticles and the nature of the Au−S bond itself have been thoroughly investigated in the last decades. Significant progress has been made in the synthesis and characterization of thiolated surfaces and nanoparticles [29, 30], whose size can be controlled with atomic resolution. Ab initio calculations, such as DFT and time dependent-DFT, have clarified many configurational aspects related to the adsorption of single thiols on flat gold surfaces and nanoparticles [79]. Stable staple-like configurations, comprising sequences of thiol-Au adatom units, (RS−Au)n, are known to stabilize thiolated surfaces and nanoparticles [30, 80] (see fig. 6.1).

Despite the available fundamental understanding of Au−S interactions and of the ground state configuration of Au-thiol interfaces, much less is known about their thermodynamics and diffusion kinetics [30]. Experimentally, thiols can self-assemble and self-organize on flat (or reconstructed) Au surfaces at temperatures slightly above room temperature [82]. Thiol diffusion has been shown to play an important role in ligand exchange reactions taking place on the surface of NPs during their synthesis process [83]. Thiol diffusion is responsible for the spontaneous, entropy-driven rearrangement of thiols of different length on the surface of Au NPs[84]. The surface patterning that derives from this spontaneous self-assembly has repercussions on the way Au NPs interact with living cells, determining their mode
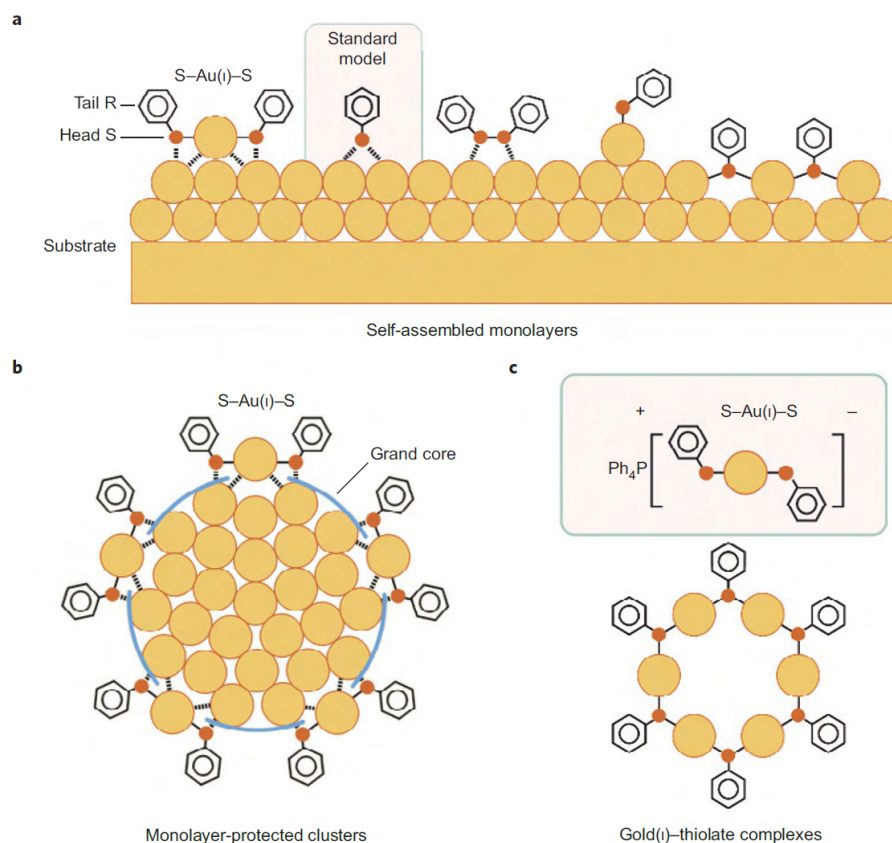
Figure 6.1: Various examples of how thiolates self assemble on fcc(111) gold surfaces (**a**), and example on NPs (**b**) and in complexes (**c**). The image is taken from refs [80, 81].

of interaction with plasma membranes [29, 85]. Furthermore, it cannot be excluded that the interaction with the biological environment can itself trigger thiol diffusion and the surface pattern reconstruction, a fact that – if proven – would have profound impact on the design of thiolated NPs with biomedical applications.

There are several reasons why thiol diffusion has not been directly tackled at computational level. The first is that *ab-initio* molecular dynamics is still limited in terms of accessible time scales, as room-temperature thiol diffusion is expected to take place on time scales of hours.

On the middle ground between *ab-initio* MD and classical MD techniques such as Density Functional based Tight Binding (DFTB) [86–88] come in to help, and some parametrization for the Au−S interaction were proposed [89]. But DFTB relies on self-consistent calculations for applying the TB theory to DFT calculated orbitals and so it generates simulations with a quasi-DFT precision, but with slow performances. A more classical

but bond-order potential, *ReaxFF* [90–92] can be used, *ReaxFF* can simulate chemical reactions via bond breaking and forming. Still, it is not as fast as classical MD but it is faster than the DFTB method and has been proved effective [93–95].

The timescale of these solutions would call for the use of lower resolution approaches, such as atomistic molecular dynamics (in combination with enhanced sampling techniques). But other bottlenecks are on the way. The first is the Au−Au model interaction. Lennard–Jones (LJ) potentials are the standard model for non bonded, Van der Waals interactions of liquids, both organic and inorganic. Au surfaces and nanoparticles with biomedical applications are expected to interact with a liquid environment. Unfortunately, two-body potentials such as LJ can not capture the characteristic bond order–bond length correlation in metals [96]. This many–body effect drives the reconstruction of Au surfaces, it contributes to the stability of the size–dependent structure of nanoparticles, and affects Au on Au diffusion processes. Many body potentials such as the Gupta [32] potential described in chapter 3 are more appropriate to the description of Au with atomistic resolution. Their implementation into parallel MD software, such as Gromacs or LAMMPS, though, is not available. A possible approach to the description of Au−Au interactions is the use of two–body polarizable Au−Au potentials, such as GolP [97, 98]. Charge transfer can indeed affect the adsorption of organic molecules at the planar Au surface or at the surface of a gold NP. This strategy has been used to study the adsorption of organic and biological molecules at planar Au surfaces. Another bottleneck is represented by the thermally-activated diffusion of thiols or Au-thiol complexes on Au surfaces. The approach that has been used so far in MD is that of treating the Au−S interaction as a bonded interaction. The Au atom, adatom, or surface and its bound thiols are modelled as a whole molecule, described by the same, unmodifiable topology of bonds, angles and dihedrals (see section 3.4, and the description of the OPLS force field). As atomistic MD simulations are non reactive, this prevents the Au−S bond to be broken during the run and no diffusion can take place. To be able to simulate the diffusion of thiols, and allow the dynamic breaking and reforming of Au−S bonds on a Au surface, the potential should be non bonded.

Recently Zhou et al. [99] proposed a set of parameters in the style of the OPLSAA forcefield that performs simulations with a good agreement with *ab-initio* MD. But this potential

lacks the characteristic that we want to simulate in the Au-S interaction: bridge or staple formations are defined at the start of the simulation and won't evolve in new configurations.

Here, we tackle the objective of developing a new non–bonded Au−S interaction potential that allows for the MD simulation of thiol diffusion on a Au surface. Our potential will be developed and validated using the many–body Gupta potential for Au−Au interactions. The Au−S potential will have a many–body approach, as well, implicitly taking into account charge transfer effects at the Au surface [97]. In section 6.2 we describe the rationale behind the choice of the Au−S potential functional form, and its relevant parameters. The new Au−S potential will be fitted to a dataset of adsorption energies and diffusion barriers obtained via DFT calculations, which are presented in section 6.3. The fitting of the model parameters to the DFT data is described in section 6.3. Finally, in section 6.6, we describe the performance of the current version of the model, and how we plan to validate it.

6.1 GOLD COORDINATION INFLUENCES THE Au−S INTERACTION

DFT calculations have demonstrated that, on the surface of Au NPs, staple structures are stable configurations. Different types of staples are possible, but in the simplest staple complex two RS- groups are bound to a single Au adatom, as schematically shown in fig. 6.1. S–bound adatoms have also been suggested to appear in thiolated planar surfaces [30]. The favourable binding of RS- groups to adatoms suggests that the coordination of the Au atom interacting with S may play an important role at determining the strength if the interaction.

We thus aimed at proving this hypothesis by means of DFT calculations.

The simplest model for representing a gold atom with a coordination η is making small $\eta + 1$ gold clusters. In fig. 6.2 we show four simple systems in which a S−CH$_3$ molecule is bound to Au atoms with coordination 0, 1, 3, and 4. In our DFT minimizations, the methanethiol is adsorbed on top of a Au atom with increasing coordination.

We also calculated data on more complex systems in which the gold atom interacting with the sulphur is part of a surface or adsorbed on the surface (fig. 6.3).
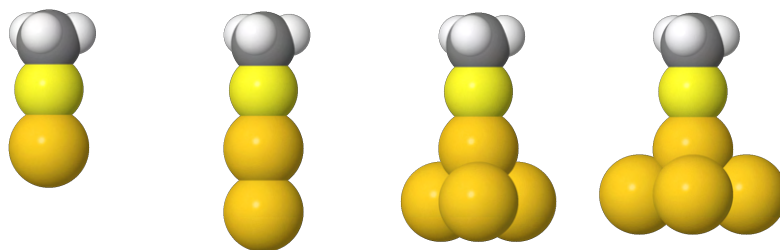
Figure 6.2: These clusters are used to determine the behaviour of the interaction as a function of the gold coordination, from left to right, the coordination of the gold atom nearest to the sulphur atom in the thiol is 0, 1, 3 and 4
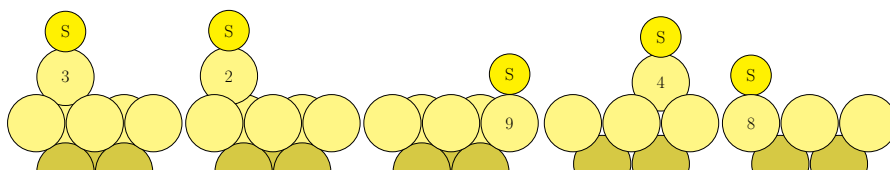

Figure 6.3: In this figure, we have indicated the coordination of the gold atoms that are closest to the sulphur in various situations. On the three left configurations, the atoms are arranged on a (111) facet, and on the two rightmost, they are on a (001) facet.

In fig. 6.4 we show how the coordination impact on the equilibrium distance as a result of the calculations on surfaces and the nanoclusters. In fig. 6.5 we present the behaviour the interaction strength. From these plots, we can conclude that both the equilibrium distance and the the Au−S interaction strength depend critically on the Au coordination. In particular, the interaction energy between a S atom and a surface is only one half of the interaction energy calculated between a S atom and a 3–coordinated Au adatom.

6.2 THE FORM OF THE POTENTIAL

To model the interaction between gold atoms and the sulphur in a thiolate we decided to use the Morse potential, like in reference [100]. The Morse potential is often used to model the interaction between atoms in molecules:

$$E(r) = \beta \left(e^{-2a(r-\sigma_0)} - 2e^{-a(r-\sigma_0)} \right) \tag{6.1}$$
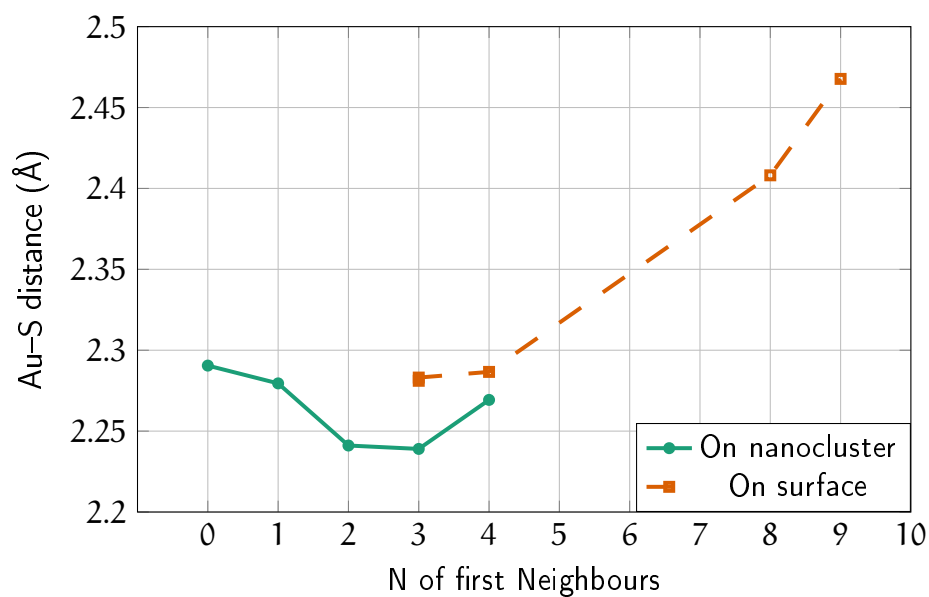
Figure 6.4: The distance between the S and the nearest Au atom obtained from the calculations.
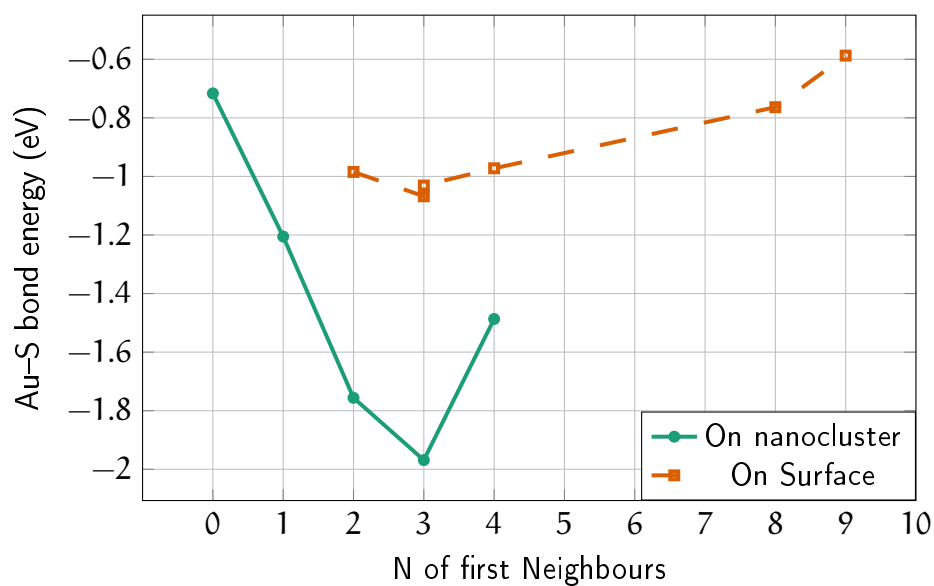

Figure 6.5: The Au−S bond energy as a function of the gold coordination in the calculations on surfaces. For the surface, at coordination $\eta = 3$ the two results correspond to having the S atom bound to an adatom adsorbed in fcc (bottom) or hcp (top) stacking.

Following the observation from section 6.1, we modelled the potential depth β and the equilibrium distance σ_0 so that they depend on the gold coordination η. We propose

$$\beta\left(\eta\right) = b_0 e^{-b_a\left(\eta^{b_b} - \eta_0\right)^2} \tag{6.2}$$

for the strength of the potential, and

$$\sigma_0\left(\eta\right) = r_0 + r_2\left(\eta - r_1\right)^2 \tag{6.3}$$

for the equilibrium distance.

One issue that needs to be dealt with is the discontinuity of η. As we aim at developing a potential to be implemented in an MD engine, the potential differentiability is desirable. For this reason, we calculate the coordination of the Au atom j as:

$$\eta_j\left(\{\mathbf{r}\}\right) = \sum_{i \neq j} f\left(\left|\mathbf{r}_j - \mathbf{r}_i\right|\right) \tag{6.4}$$

where $f\left(r\right)$ is a weight function to count the neighbours. In eq. (6.4) we assign to each atom near j the weight:

$$f\left(r\right) = \begin{cases} 1 & r < r_s \\ A_5\left(r - r_e\right)^5 + A_4\left(r - r_e\right)^4 + A_3\left(r - r_e\right)^3 & r_s \leqslant r < r_e \\ 0 & r \leqslant r_e \end{cases} \tag{6.5}$$

where A_5, A_4, A_3 are chosen in order to link 1 to 0 between r_s and r_e in a way that f and both its first and second derivative are continuous functions.

The peculiarity of this potential is the asymmetry of the form of the forces due to the dependency of η only on the coordinates of the Au atoms (see appendix A)

6.3 A DFT-BASED DATASET FOR THE FIT OF THE CLASSICAL POTENTIAL

Now that the functional form of the potential is fixed, we need to determine the parameters $a, r_0, r_2, r_1, b_0, b_a, b_b$ and η_0 for the equations (6.1), (6.2) and (6.3). We decided to fit these parameters on a database of configurations of a single methanethiol adsorbed on a gold surface.

As a first step, we selected 34 points on the (x,y) plane of a (111) Au surface, 23 points on the (x,y) plane of a (100) surface, 30 points on the (x,y) plane of a (111) surface containing an

adatom, and 14 points on the (x,y) plane of a (100) surface containing an adatom. The whole set of these coordinates is shown in fig. 6.6. The choice of these positions has been driven by the need to represent:

- favourable adsorption sites, which usually correspond to hollow sites. On the (111) surface, for instance, we considered both fcc and hcp adsorption sites;

- bridge configurations, in which the thiol bridges two gold atoms;

- unfavourable adsorption sites, such as the on top configurations.

The choice of such a large and variegated set of configurations should be functional to the delivery of a classical potential able to describe realistically the diffusion of thiols on surfaces.

Once the total number of 101 (x,y) points had been identified, for each of these points we optimized the thiol z coordinate. In this optimization, we fixed the coordinates of the gold atoms, the x and y coordinate of the S and the C atoms and let the rest of the system ($Au-S$, $S-C$ distances, $C-H$ distances and orientation) relax. In this way, we obtained a relaxed thiol placed perpendicularly on the gold surface in the chosen (x,y) position. We also optimized an isolated SCH_3 that we used as a reference in the construction of the fitting set.

We then completed our DFT-based dataset using a series of single-point energy calculations. For each of the (x,y) positions shown in fig. 6.6, we calculated the adsorption energy of the reference thiol by varying its z coordinate by 0.0 Å, ±0.05 Å, ±0.10 Å, ±0.15 Å, ±0.25 Å, ±0.35 Å with respect to the minimum energy configuration. In these calculations, the internal geometry of the thiol was kept fixed and identical to that of the minimized, isolated thiol. Figure 6.7 shows the dependence of the interaction energy on z, for a restricted set of configurations.

The interaction energy from the DFT results is calculated with this formula:

$$E^{DFT}_{Au-SCH_3} = E^{DFT}_{tot} - E^{DFT}_{thiol} - E^{DFT}_{Au} \tag{6.6}$$

Where $E^{DFT}_{Au-SCH_3}$ is the interaction energy between the gold of the surface and the sulphur of the thiol plus a long term contribution due to the methyl, E^{DFT}_{tot} is the total energy that we get from the DFT calculations, E^{DFT}_{thiol} is the energy of the reference SCH_3 and E^{DFT}_{Au} is the energy of the gold surface alone.
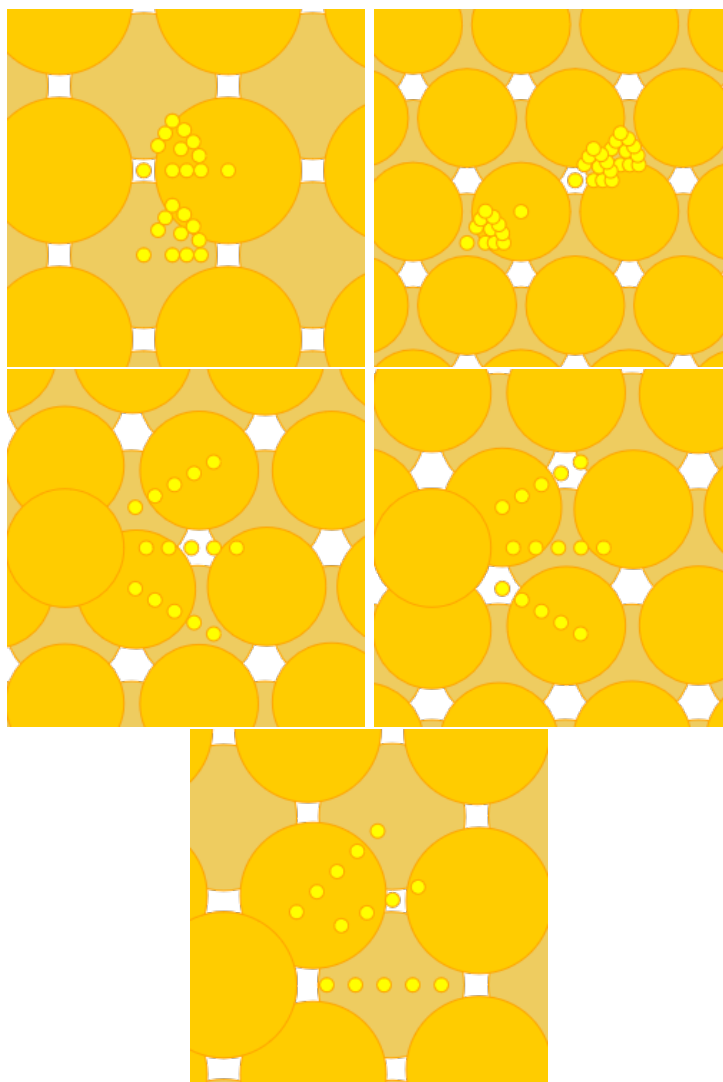
Figure 6.6: The various configuration used in the fit set. The light yellow dots represent the position of the thiols in the various configurations. On the top row there are the naked (001) and (111) surfaces, and on the second row, from the left, the (111) surface with an adatom on the fcc and the hcp sites, on the third row we have the (001) surface with an adatom.
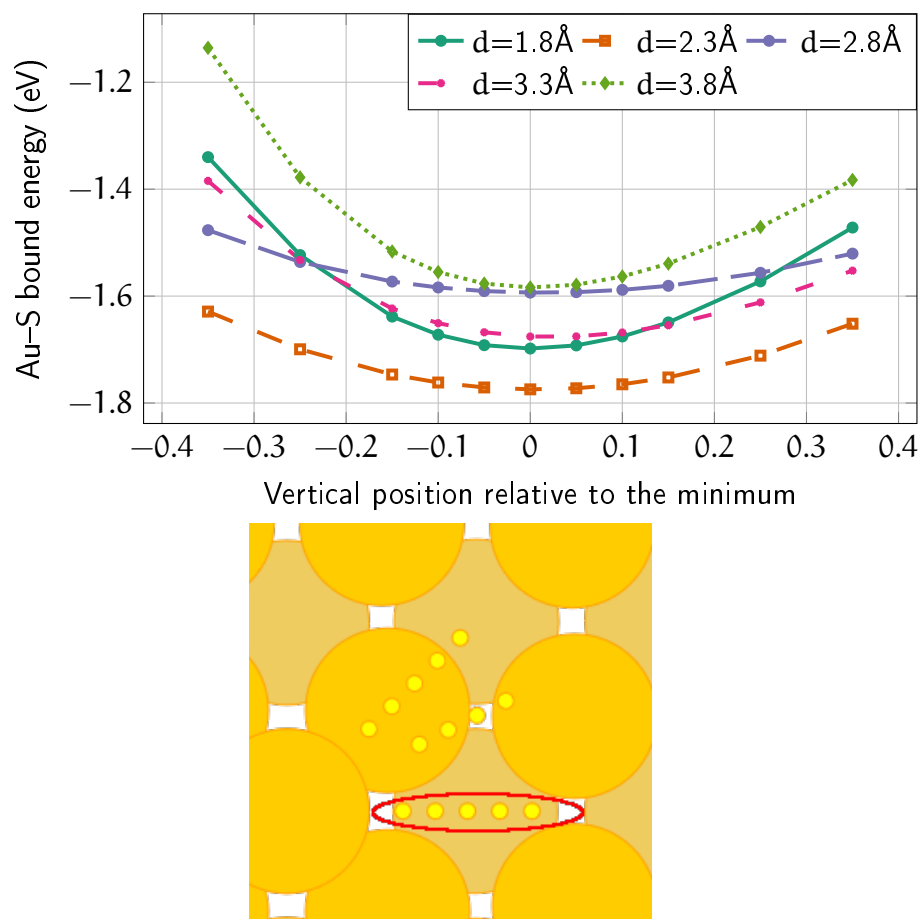
Figure 6.7: An example of the *z*-dependence of the Au−S interaction energy of some configuration in the fit set. The energies are taken from the (001) surface with an adatom. The d in the legend represent the horizontal distance from the adatom.

Since the classical energy given by eq. (6.1) only provides the interaction energy between the sulphur and the gold atoms, for fitting purposes we considered the whole thiol energy $E_{Au-thiol}^{MD}$ as the sum of the interaction Au−S due to eq. (6.1) and the interaction Au−CH_3. To calculate the interaction between the carbon and the gold surface we decided to use the LJ 12–6 potential. The energy is calculated by using the parameters from the force field OPLSUA [33] for the CH_3 and the parameters of the "LJ gold" proposed by Heinz [101]:

$$E_{Au-thiol}^{MD} = E_{Au-S}^{MD} + E_{Au-C}^{MD} \tag{6.7}$$

where, for the fit, the Au−CH_3 interaction E_{Au-C}^{MD} is known, and the gold–sulphur interaction E_{Au-S}^{MD} is calculated by the fitting parameters.

6.4 FITTING PROCEDURE AND RESULTS

We used the PSO algorithm (see section 1.2) to fit the parameters a, r_0, r_2, r_1, b_0, b_a, b_b and η_0 of eqs. (6.1) to (6.3). We applied the PSO to a population of particles made between 4^8 and 5^8 individuals to cover a large number of combination of parameters. The function that the PSO algorithm minimized was the sum of the squared errors between the DFT energy from eq. (6.6) and the classical energy from eq. (6.7) calculated for each configuration of the fit set. Each ith configuration contributed to the sum with:
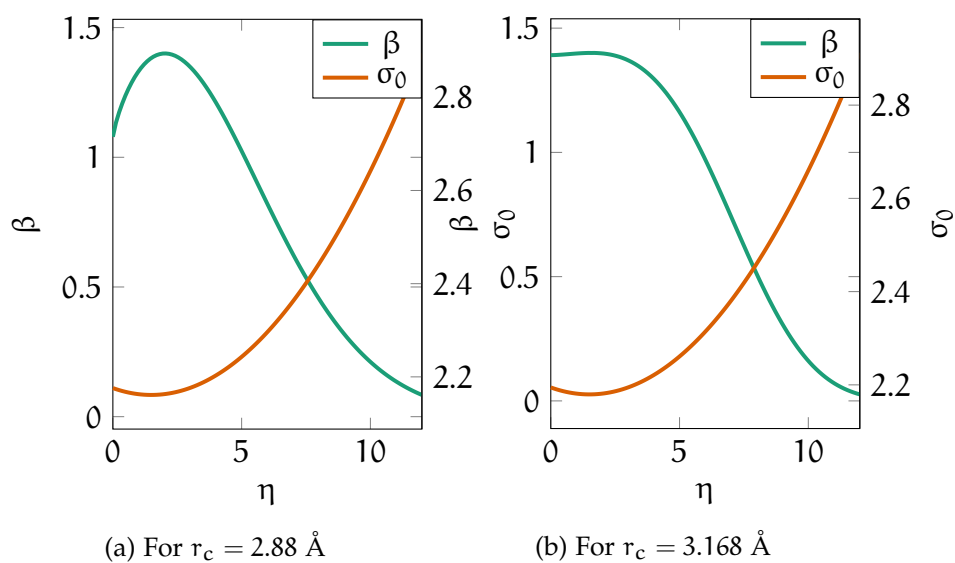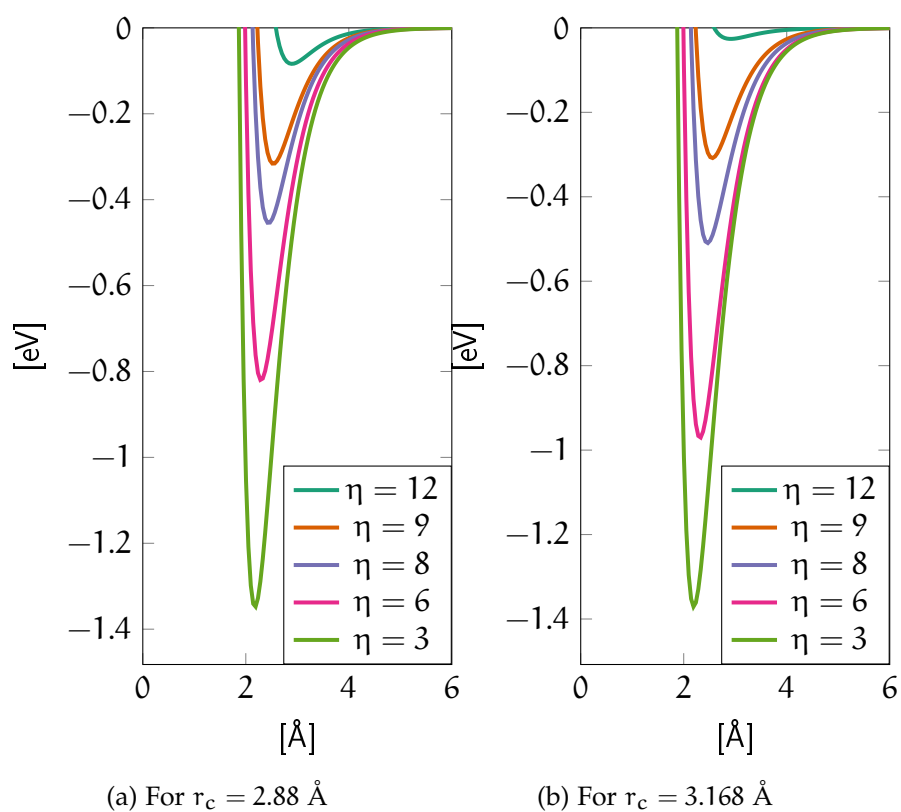
$$w_i = \left(E^{MD}_{Au-thiol} - E^{DFT}_{Au-thiol}\right)^2 \tag{6.8}$$

Table 6.1 and figs. 6.8 and 6.9 present the result of two different fit with different settings for calculating η (see (6.5)): for the first fit we used $r_c = 2.88$ Å and $r_e = 3.2$ Å, for the second $r_c = 3.168$ Å and $r_e = 3.52$ Å. The values of r_c and r_e in the second set are 10 % bigger that the respective values of the first set. We thought that the second relaxed set should take better care of thermal oscillations of the gold atoms during the MD simulations. In both the fits b_0 has been capped at 1.4 eV.

Parameter	$r_c = 2.88$ Å	$r_c = 3.168$ Å
$b_0[eV]$	1.4	1.4
b_a	0.0823754	0.00153155
b_b	0.817473	1.59807
η_0	1.77902	2.0573
$r_0[Å]$	2.16121	2.17954
r_1	1.49042	1.5
$r_2[Å]$	0.00663653	0.00664493
$a[Å^{-1}]$	2.22523	2.15515

Table 6.1: The results of the fit for two different parameters for calculating η. The parameters b_a, b_b, η_0 and r_1 are dimensionless, see eqs. (6.2) and (6.3)

Qualitatively, the trend of β is such that the interaction with the lowest coordinated atoms, and adatoms in particular, is larger than that with surface Au atoms. This larger interaction comes along with a contraction of the Au−S equilibrium distance. Figure 6.9 shows the dependence of the potential shape on the Au coordination. In the next paragraph we report our latest results on the model validation.

(a) For $r_c = 2.88$ Å

(b) For $r_c = 3.168$ Å

Figure 6.8: The shape of σ and β for the fit results.

(a) For $r_c = 2.88$ Å

(b) For $r_c = 3.168$ Å

Figure 6.9: The AuS interaction at various values of η for the two fits.

6.5 LAMMPS IMPLEMENTATION

We used LAMMPS [31] (lammps.sandia.gov) to perform the MD simulations. I implemented both the SMATB potential and also the Au−S interaction potential into LAMMPS.

LAMMPS is modular and so a developer can implement her tools that can be used during a simulation. The tools can be potentials that are not included in the release of LAMMPS or even analysis routines or integrators. Within LAMMPS the potentials are called "*pairs*" and the other tools that can be implemented are defined as "*fixes*".

The SMATB potential, even if it is a manybody potential due to the form of the bonding energy, needs only the implementation of a new "pair" routine. On the contrary, the Au−S with its asymmetric bond order dependency needs a more complex implementation with a "*pair*" routine supported by a "*fix*" routine that calculates the gold coordination and updates the Morse parameters at each simulation step.

6.6 MOLECULAR DYNAMICS

With the potential implemented in LAMMPS we started a few preliminary MD simulations. The aim of these simulations is to confirm the stability of the potential and the correctness of the implementation.

The simulation settings are:

- timestep: 2 fs

- thermostat: langevin set at 300 K, included in LAMMPS

- the interaction parameters for the S atoms and the CH_3 beads from OPLS, with the relative mixing rules

- the interaction between the Au atoms is the SMATB potential[1]

- the interaction between Au atoms and CH_3 beads is a LJ 12–6 potential[2]

- the interaction Au−S is described by our new potential

---

[1] The parameters of the potential we used comes from a private communication by Riccardo Ferrando, and are fitted in order to behave with slightly more long range interaction than for example the ones in ref [66]

[2] We are using the OPLS mixing rules between the CH_3 OPLS parameters an the Au LJ 12–6 parameters proposed by Heinz [101].

Even if plain Au (111) surfaces tend to reconstruct in an herringbone superstructure [102], we decided to approach the first simulations with the simplest configurations possible, a plain surface. This choice is coherent with the DFT database used for the parameter optimization. Before starting each simulation we minimized locally the system with the default minimization algorithm included in LAMMPS.

In this section we will present the results of simulations made with the parameters taken from the two settings presented in table 6.1.

(a) Start for $r_c = 2.88$

(b) Start for $r_c = 3.168$

(c) $r_c = 2.88$ after 200 ns
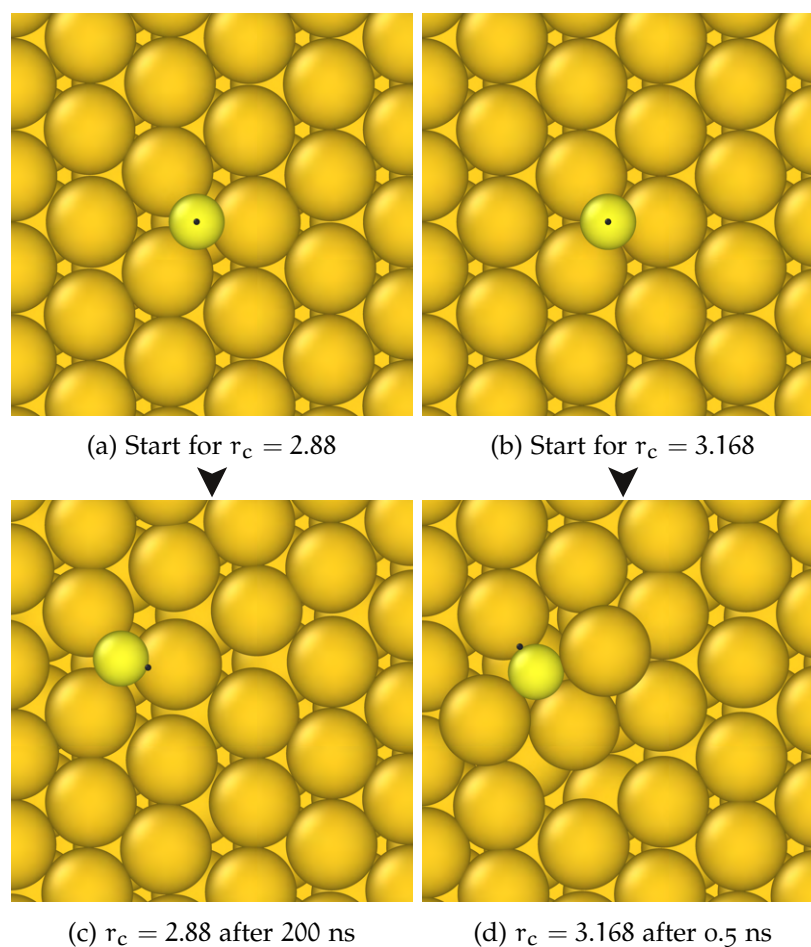
(d) $r_c = 3.168$ after 0.5 ns

Figure 6.10: The starting configurations and a snapshot of the simulation on (111) surfaces for both the parameter set taken into account. The gold surfaces are in the darker shade of yellow. The S atoms are light yellow and the CH_3 beads are the small black spheres.

On the plain fcc(111) surfaces (figs. 6.10 to 6.12) the results show an unexpected higher aggressiveness of the potential fitted with the more relaxed condition on the gold coordination η (with
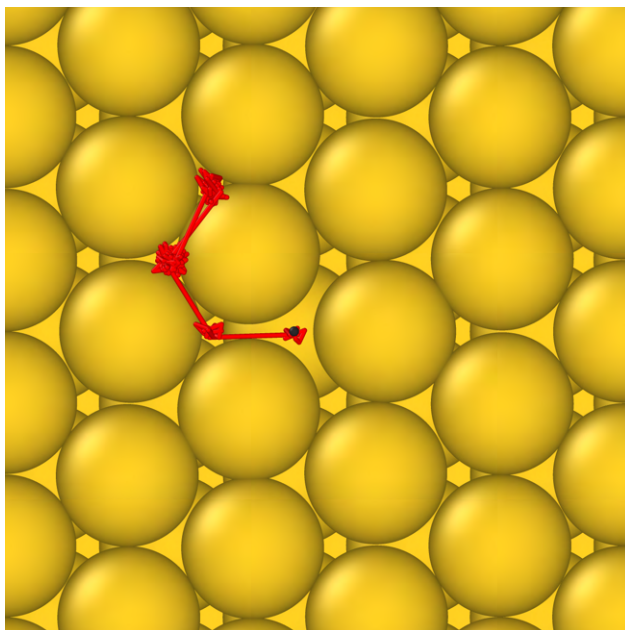
Figure 6.11: The trajectory of a single thiol on a 111 surface, with $r_c = 2.88$. During the 200 ns simulation the thiol have hopped 4 times between adsorptions sites, the third site is visited two times during the diffusion. The trajectory is in red, the surface and the thiol are pictured at the *start* of the simulation and the atoms of the thiol are represented as small spheres for clarity.
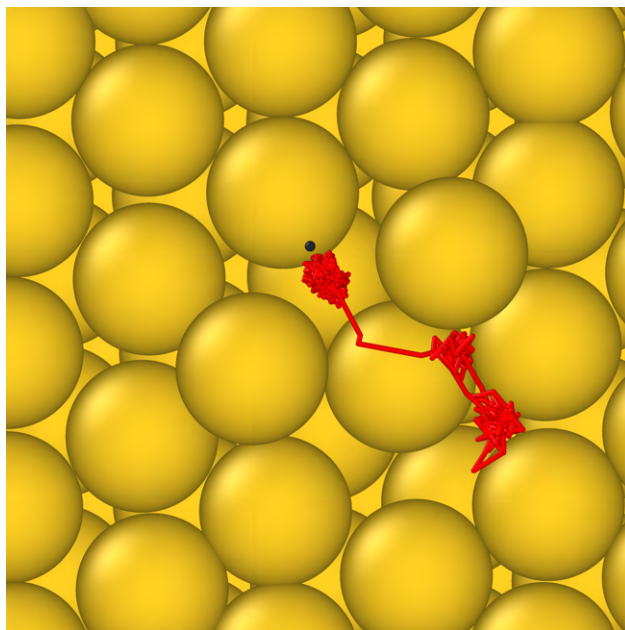
Figure 6.12: The trajectory of a single thiol on a 111 surface with $r_c = 3.168$. During the 0.5 ns simulation the thiol have hopped 4 times between adsorptions sites, the first site is visited two times during this diffusion. In this case the thiol disrupts the surface more than in fig. 6.11 and it even lifts a gold atom from the surface. The trajectory is in red, the surface and the thiol are pictured at the *final* snapshot of the simulation and the atoms of the thiol are represented as small spheres for clarity.

$r_c = 3.168$ Å and $r_e = 3.53$ Å, see (6.5)) than in the one fitted whit the more strict parameters. The atom dislodged in fig. 6.10d is lifted from the surface near the end of the simulation, after the last diffusion event of the thiol.

(a) Start for $r_c = 2.88$

(b) Start for $r_c = 3.168$

(c) $r_c = 2.88$ after 0.5 ns
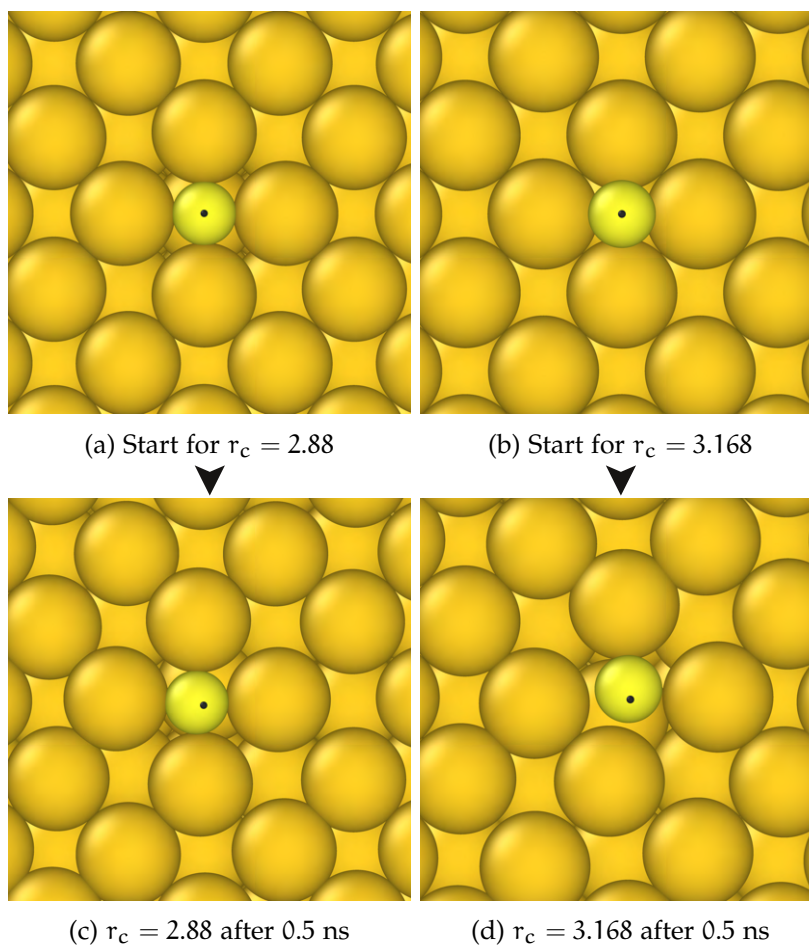
(d) $r_c = 3.168$ after 0.5 ns

Figure 6.13: The starting configurations and a snapshot of the simulation on (001) surfaces for both the parameter set taken into account. In this case the difference is more evident after the minimization: in **b** the four Au atoms are more packed at the base of the S· The gold surfaces are in the darker shade of yellow. The S atoms are light yellow and the CH_3 beads are the small black spheres.

On the plain fcc(001) surfaces (fig. 6.13) the results confirm the higher tendency for the S to attract Au atoms in the potential fitted with $r_c = 3.168$ Å (see (6.5)). On the (001) surfaces we did not observe any diffusion of the thiol nor any significant disruption of the gold surface.

Our MD simulations, aimed at validation of our classical potential, are still ongoing at the time of writing. In the last paragraph,

we have shown that the tendency of S−CH$_3$ to disrupt the Au surface is very sensitive to the choice of the potential parameters. It is crucial, then, to identify the most appropriate experimental data to validate our approach and choose the parameterization that better agrees with experiments.

7

SUMMARY AND OUTLOOK

In the first part of my Thesis I developed different global optimization tools. These tools have been successfully used for different purposes, as summarized here.

As a continuation the work of my Master Thesis, I improved the previous BH code by rewriting it in C++, in order to make it more flexible and user-friendly. This has been possible by exploiting the features of the C++ language.

This new code, BH++, has been used with an interface with the DFT packages QUANTUM Espresso and CP2K to perform BH searches at the *ab initio* level. This type of global optimization search is very important for the systems in which existing atomistic force fields give poor results, as for example in AgAu [103] which was treated in my Master Thesis, and in those systems in which the DFT data may serve to develop new force fields. Moreover, DFT global optimization searches are a powerful tool to interpret experimental results about the equilibrium structures of nanoparticles. In my PhD Thesis, I used the BH–DFT interface to investigate whether the experimentally observed L1$_1$@Ag-skin structures of AgPt nanoparticles were corresponding to the optimal chemical ordering configurations. This work has been done in collaboration with the experimental group of the University of Orléans (Jérome Pirart, Pascal Andreazza and Caroline Andreazza-Vignolle) and with the computational group of CINaM/CNRS in Marseille (Alexis Front and Christine Mottet) who performed Monte Carlo simulations by atomistic force fields. The results of this work revealed a quite peculiar behaviour of the L1$_1$@Ag-skin phase, which is stable only at very small NPs sizes, while it breaks at large sizes. The results are published in Nature Communications [24].

The BH–DFT is now available for further studies of chemical optimization of different nanoalloys systems, including ternary ones, as AuPtPd studied in Ref. [104].

The modular nature of BH++ make it possible to implement and test new optimization algorithms with relative ease. This feature allowed us to develop a new optimization algorithm, the Flying Landing (F/L) algorithm, with the aim of more efficiently optimizing both geometric shape and chemical ordering

of nanoalloys within the same search. The F/L algorithm has been tested in the optimization of AuRh and AuCu NPs of size 400 atoms, for which the comparison with results in the literature was possible. These tests have already shown that the F/L algorithm is clearly more efficient than standard BH. Other tests are under way. A further development of the F/L algorithm is being made now to include a third type of specialized walker for an even better refinement of chemical ordering.

Global optimization has been used not only for the search of optimal structures of nanoalloys, but also in the fitting of the Au−S interaction potential. To this end, the PSO global optimization algorithm has been developed and used. The Au−S classical interaction potential has been developed with the aim of using it in large-scale MD simulations of thiolates on gold surfaces, and in particular on the surface of golden NPs. These simulations would bee too cumbersome to be made at the DFT level so that the atomistic force field is likely to be quite useful.

To develop the Au−S interaction potential we performed a large set of DFT calculations in order to build up a database of configurations of methanetiolates on fcc(111) and fcc(001) Au surfaces. This collection of configurations has been used to fit the parameters of the Au−S force field, which has been then tested in MD simulations of thiols on these flat, high-symmetry Au surfaces.

In order to perform these MD simulations, I have implemented in LAMMPS, that is an excellent program for prototyping force fields, the SMATB potential along with the AU−S interaction. I have written a simple walk-through for implementing a *pair* style (a potential) in LAMMPS[1]. We plan to further develop the work on the Au−S interactions by making tests on surfaces with defects. Depending on the results of these new simulations, I will also consider to introduce angular terms in the Au−S interaction to better describe the directional parts of the Au−S interactions.

---

[1] The guide is available at the link https://www.overleaf.com/read/jgntdbqmtrty

Part IV

APPENDIX

THE Au−S FORCES

For the sake of calculations in this chapter we will use in formulas uppercase letter for indicating sulphur and lowercase for indicating gold, so that, for example, $\{\mathbf{R}\}$ are the coordinates of sulphur atoms and $\{\mathbf{r}\}$ the ones of gold atoms.

If we combine eqs. (6.1) to (6.3) in:

$$E^{AuS}\left(\{\mathbf{R}\},\{\mathbf{r}\}\right) =$$
$$\sum_{I,i} \beta\left(\eta_i\left(\{\mathbf{r}\}\right)\right)\left(e^{-a\left(|\mathbf{R}_I-\mathbf{r}_i|-\sigma_0\left(\eta_i\left(\{\mathbf{r}\}\right)\right)\right)} - 2e^{-2a\left(|\mathbf{R}_I-\mathbf{r}_i|-\sigma_0\left(\eta_i\left(\{\mathbf{r}\}\right)\right)\right)}\right)$$

$$\text{(A.1)}$$

For the sake of brevity we will use

$$\mathcal{E}_{Ii} = \left(e^{-a\left(|\mathbf{R}_I-\mathbf{r}_i|-\sigma_0\left(\eta_i\left(\{\mathbf{r}\}\right)\right)\right)} - 2e^{-2a\left(|\mathbf{R}_I-\mathbf{r}_i|-\sigma_0\left(\eta_i\left(\{\mathbf{r}\}\right)\right)\right)}\right) \quad \text{(A.2)}$$

and

$$d\mathcal{E}_{Ii} = \left(e^{-2a\left(|\mathbf{R}_I-\mathbf{r}_i|-\sigma_0\left(\eta_i\left(\{\mathbf{r}\}\right)\right)\right)} - e^{-a\left(|\mathbf{R}_I-\mathbf{r}_i|-\sigma_0\left(\eta_i\left(\{\mathbf{r}\}\right)\right)\right)}\right) \quad \text{(A.3)}$$

The force acting on the sulphur atoms S has this form:

$$\frac{\partial E^{AuS}\left(\{\mathbf{R}\},\{\mathbf{r}\}\right)}{\partial \mathbf{R}_S} = -2a\sum_i \beta\left(\eta_i\left(\{\mathbf{r}\}\right)\right)d\mathcal{E}_{Si}\frac{\mathbf{R}_S-\mathbf{r}_i}{|\mathbf{R}_S-\mathbf{r}_i|} \quad \text{(A.4)}$$

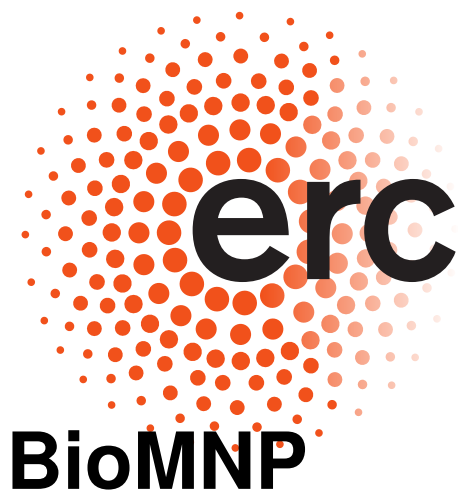Where $\Delta_{Ii} = \mathbf{R}_I - \mathbf{r}_i$ is a vectorial quantity.

An the forces acting on the gold atoms:

$$\frac{\partial E^{AuS}\left(\{\mathbf{R}\},\{\mathbf{r}\}\right)}{\partial \mathbf{r}_k} =$$
$$= -2a\sum_I \beta\left(\eta_k\left(\{\mathbf{r}\}\right)\right)\frac{\mathbf{r}_k-\mathbf{R}_I}{|\mathbf{R}_I-\mathbf{r}_k|}d\mathcal{E}_{Ik}$$
$$+ \sum_I\sum_i \frac{\partial\eta_i\left(\{\mathbf{r}\}\right)}{\partial\mathbf{r}_k}\left(-\mathcal{E}_{Ii}\left.\frac{\partial\beta\left(n\right)}{\partial n}\right|_{\left(n=\eta_i\left(\{\mathbf{r}\}\right)\right)}\right.$$
$$\left.+2a\beta\left(\eta_i\left(\{\mathbf{r}\}\right)\right)d\mathcal{E}_{Ii}\left.\frac{\partial\sigma_0\left(n\right)}{\partial n}\right|_{\left(n=\eta_i\left(\{\mathbf{r}\}\right)\right)}\right) \quad \text{(A.5)}$$

ACKNOWLEDGEMENT FOR FUNDING

[1] Oleg V Salata. "Applications of nanoparticles in biology and medicine." In: *Journal of nanobiotechnology* 2.1 (Apr. 2004). ISSN: 1477-3155. DOI: 10.1186/1477-3155-2-3. URL: https://doi.org/10.1186/1477-3155-2-3.

[2] Wenbin Lin. "Introduction: Nanoparticles in Medicine." In: *Chemical Reviews* 115.19 (2015), pp. 10407–10409. ISSN: 15206890. DOI: 10.1021/acs.chemrev.5b00534.

[3] Didier Astruc. "Introduction: Nanoparticles in Catalysis." In: *Chemical Reviews* 120.2 (Jan. 2020), pp. 461–463. ISSN: 0009-2665. DOI: 10.1021/acs.chemrev.8b00696. URL: https://pubs.acs.org/doi/10.1021/acs.chemrev.8b00696.

[4] Jaison Jeevanandam, Ahmed Barhoum, Yen S Chan, Alain Dufresne, and Michael K Danquah. "Review on nanoparticles and nanostructured materials: history, sources, toxicity and regulations." In: *Beilstein Journal of Nanotechnology* 9 (Apr. 2018), pp. 1050–1074. ISSN: 2190-4286. DOI: 10.3762/bjnano.9.98. URL: https://www.beilstein-journals.org/bjnano/articles/9/98.

[5] A.P. Guimaraes. *Principles of Nanomagnetism*. Springer, Berlin, 2009.

[6] Jacob D. Gibson, Bishnu P. Khanal, and Eugene R. Zubarev. "Paclitaxel-Functionalized Gold Nanoparticles." In: *Journal of the American Chemical Society* 129.37 (Sept. 2007), pp. 11653–11661. ISSN: 0002-7863. DOI: 10.1021/ja075181k. URL: https://pubs.acs.org/doi/10.1021/ja075181k.

[7] Cláudia Saraiva, Catarina Praça, Raquel Ferreira, Tiago Santos, Lino Ferreira, and Liliana Bernardino. "Nanoparticle-mediated brain drug delivery: Overcoming blood–brain barrier to treat neurodegenerative diseases." In: *Journal of Controlled Release* 235 (Aug. 2016), pp. 34–47. ISSN: 01683659. DOI: 10.1016/j.jconrel.2016.05.044. URL: https://linkinghub.elsevier.com/retrieve/pii/S0168365916303236.

[8]   Yuanzeng Min, Joseph M. Caster, Michael J. Eblan, and Andrew Z. Wang. "Clinical Translation of Nanomedicine." In: *Chemical Reviews* 115.19 (2015), pp. 11147–11190. ISSN: 15206890. DOI: 10.1021/acs.chemrev.5b00116.

[9]   Mahmoud Elsabahy, Gyu Seong Heo, Soon Mi Lim, Guorong Sun, and Karen L. Wooley. "Polymeric Nanostructures for Imaging and Therapy." In: *Chemical Reviews* 115.19 (2015), pp. 10967–11011. ISSN: 15206890. DOI: 10.1021/acs.chemrev.5b00135.

[10]   Darrell J. Irvine, Melissa C. Hanson, Kavya Rakhra, and Talar Tokatlian. "Synthetic Nanoparticles for Vaccines and Immunotherapy." In: *Chemical Reviews* 115.19 (2015), pp. 11109–11146. ISSN: 15206890. DOI: 10.1021/acs.chemrev.5b00109.

[11]   Subinoy Rana, Avinash Bajaj, Rubul Mout, and Vincent M. Rotello. "Monolayer coated gold nanoparticles for delivery applications." In: *Advanced Drug Delivery Reviews* 64.2 (Feb. 2012), pp. 200–216. ISSN: 0169409X. DOI: 10.1016/j.addr.2011.08.006. URL: https://linkinghub.elsevier.com/retrieve/pii/S0169409X11002316.

[12]   Rachel S. Riley and Emily S. Day. "Gold nanoparticle-mediated photothermal therapy: applications and opportunities for multimodal cancer treatment." In: *Wiley Interdisciplinary Reviews: Nanomedicine and Nanobiotechnology* 9.4 (July 2017), e1449. ISSN: 19395116. DOI: 10.1002/wnan.1449. URL: http://doi.wiley.com/10.1002/wnan.1449.

[13]   Riccardo Ferrando, Julius Jellinek, and Roy L Johnston. "Nanoalloys: From Theory to Applications of Alloy Clusters and Nanoparticles." In: *Chemical Reviews* 108.3 (Mar. 2008), pp. 845–910. ISSN: 0009-2665. DOI: 10.1021/cr040090g. URL: http://dx.doi.org/10.1021/cr040090g%20https://pubs.acs.org/doi/10.1021/cr040090g.

[14]   R. Ferrando. *Structure and Properties of Nanoalloys*. Frontiers of Nanoscience, Volume 10. Elsevier, 2016.

[15]   J. A. Alonso. *Structure and Properties of Atomic Nanoclusters*. Imperial College Press, 2005.

[16]   R. L. Johnston. *Atomic and Molecular Clusters*. Taylor and Francis, London, 2002.

[17]   D. J. Wales. *Energy Landscapes*. Cambridge University Press, 2003.

[18] G. Rossi, A. Rapallo, C. Mottet, A. Fortunelli, F. Baletto, and R. Ferrando. "Magic Polyicosahedral Core-Shell Clusters." In: *Phys. Rev. Lett.* 93 (2004), p. 105503.

[19] D. J. Wales and J. P. K. Doye. "Global optimization by Basin-Hopping and the Lowest Energy Structures of Lennard-Jones Clusters Containing up to 110 Atoms." In: *J. Phys. Chem. A* 101 (1997), pp. 5111–5116.

[20] Giulia Rossi and Riccardo Ferrando. "Global optimization by excitable walkers." In: *Chemical Physics Letters* 423.1-3 (May 2006), pp. 17–22. ISSN: 00092614. DOI: 10.1016/j.cplett.2006.03.003. URL: https://linkinghub.elsevier.com/retrieve/pii/S0009261406003186.

[21] Giulia Rossi and Riccardo Ferrando. "Searching for low-energy structures of nanoparticles: a comparison of different methods and algorithms." In: *Journal of Physics: Condensed Matter* 21.8 (Feb. 2009), p. 084208. ISSN: 0953-8984. DOI: 10.1088/0953-8984/21/8/084208. URL: http://stacks.iop.org/0953-8984/21/i=8/a=084208%20https://iopscience.iop.org/article/10.1088/0953-8984/21/8/084208.

[22] Paolo Giannozzi et al. "QUANTUM ESPRESSO: a modular and open-source software project for quantum simulations of materials." In: *Journal of Physics: Condensed Matter* 21.39 (2009), p. 395502.

[23] Thomas D. Kühne et al. "CP2K: An electronic structure and molecular dynamics software package - Quickstep: Efficient and accurate electronic structure calculations." In: *The Journal of Chemical Physics* 152.19 (May 2020), p. 194103. ISSN: 0021-9606. DOI: 10.1063/5.0007045. arXiv: 2003.03868. URL: https://doi.org/10.1063/5.0007045%20http://aip.scitation.org/doi/10.1063/5.0007045.

[24] Jérome Pirart, Alexis Front, Daniele Rapetti, Caroline Andreazza-Vignolle, Pascal Andreazza, Christine Mottet, and Riccardo Ferrando. "Reversed size-dependent stabilization of ordered nanophases." In: *Nature Communications* 10.1 (Dec. 2019), p. 1982. ISSN: 2041-1723. DOI: 10.1038/s41467-019-09841-3. URL: http://www.nature.com/articles/s41467-019-09841-3.

[25] Michael L. Etheridge, Stephen A. Campbell, Arthur G. Erdman, Christy L. Haynes, Susan M. Wolf, and Jeffrey McCullough. "The big picture on nanomedicine: the state of investigational and approved nanomedicine products." In: *Nanomedicine: Nanotechnology, Biology and Medicine* 9.1 (Jan. 2013), pp. 1–14. ISSN: 15499634. DOI: 10.1016/j.nano.2012.05.013. URL: http://dx.doi.org/10.1016/j.nano.2012.05.013%20https://linkinghub.elsevier.com/retrieve/pii/S1549963412002882.

[26] Anil Desireddy et al. "Ultrastable silver nanoparticles." In: *Nature* 501.7467 (Sept. 2013), pp. 399–402. ISSN: 0028-0836. DOI: 10.1038/nature12523. URL: http://www.nature.com/articles/nature12523.

[27] Hind Al-Johani et al. "The structure and binding mode of citrate in the stabilization of gold nanoparticles." In: *Nature Chemistry* 9.9 (Sept. 2017), pp. 890–895. ISSN: 1755-4330. DOI: 10.1038/nchem.2752. URL: http://www.nature.com/articles/nchem.2752.

[28] Tatu Lajunen et al. "Light induced cytosolic drug delivery from liposomes with gold nanoparticles." In: *Journal of Controlled Release* 203 (Apr. 2015), pp. 85–98. ISSN: 01683659. DOI: 10.1016/j.jconrel.2015.02.028. URL: https://linkinghub.elsevier.com/retrieve/pii/S0168365915001388.

[29] Paolo Pengo et al. "Gold nanoparticles with patterned surface monolayers for nanomedicine: current perspectives." In: *European Biophysics Journal* 46.8 (Dec. 2017), pp. 749–771. ISSN: 0175-7571. DOI: 10.1007/s00249-017-1250-6. URL: http://link.springer.com/10.1007/s00249-017-1250-6.

[30] Thomas Bürgi. "Properties of the gold–sulphur interface: from self-assembled monolayers to clusters." In: *Nanoscale* 7.38 (2015), pp. 15553–15567. ISSN: 2040-3364. DOI: 10.1039/C5NR03497C. URL: http://xlink.rsc.org/?DOI=C5NR03497C.

[31] Steve Plimpton. "Fast Parallel Algorithms for Short-Range Molecular Dynamics." In: *Journal of Computational Physics* 117.1 (Mar. 1995), pp. 1–19. ISSN: 00219991. DOI: 10.1006/jcph.1995.1039. URL: https://linkinghub.elsevier.com/retrieve/pii/S002199918571039X.

[32] Raju P. Gupta. "Lattice relaxation at a metal surface." In: *Phys. Rev. B* 23 (12 June 1981), pp. 6265–6270. DOI: 10.1103/PhysRevB.23.6265. URL: https://link.aps.org/doi/10.1103/PhysRevB.23.6265.

[33] William L. Jorgensen and Julian Tirado-Rives. "The OPLS [optimized potentials for liquid simulations] potential functions for proteins, energy minimizations for crystals of cyclic peptides and crambin." In: *Journal of the American Chemical Society* 110.6 (Mar. 1988), pp. 1657–1666. ISSN: 0002-7863. DOI: 10.1021/ja00214a001. URL: http://pubs.acs.org/doi/abs/10.1021/ja00214a001.

[34] James Kennedy and Russell Eberhart. "Particle swarm optimization." In: *Proceedings of ICNN'95 - International Conference on Neural Networks*. Vol. 4. IEEE, 1995, pp. 1942–1948. ISBN: 0-7803-2768-3. DOI: 10.1109/ICNN.1995.488968. URL: http://ieeexplore.ieee.org/document/488968/.

[35] G. Rossi and R. Ferrando. "Searching for low-energy structures of nanoparticles: a comparison of different methods and algorithms." In: *J. Phys. Cond. Mat.* 21 (2009), p. 084208.

[36] D. Bochicchio and R. Ferrando. "Size-Dependent Transition to High-Symmetry Chiral Structures in AgCu, AgCo, AgNi, and AuNi Nanoalloys." In: *Nano Lett.* 10 (2010), pp. 4211–4216.

[37] D. Bochicchio and R. Ferrando. "Morphological instability of core-shell metallic nanoparticles." In: *Phys. Rev. B* 87 (2013), p. 165435.

[38] Giulia Rossi and Riccardo Ferrando. "Combining shape-changing with exchange moves in the optimization of nanoalloys." In: *Computational and Theoretical Chemistry* 1107 (May 2017), pp. 66–73. ISSN: 2210271X. DOI: 10.1016/j.comptc.2017.01.002. URL: http://dx.doi.org/10.1016/j.comptc.2017.01.002%20https://linkinghub.elsevier.com/retrieve/pii/S2210271X17300026.

[39] J. Dana. Honeycutt and Hans C. Andersen. "Molecular dynamics study of melting and freezing of small Lennard-Jones clusters." In: *The Journal of Physical Chemistry* 91.19 (1987), pp. 4950–4963. DOI: 10.1021/j100303a014. eprint: http://dx.doi.org/10.1021/j100303a014. URL: http://dx.doi.org/10.1021/j100303a014.

[40]   Daniel Faken and Hannes Jónsson. "Systematic analysis of local atomic structure combined with 3D computer graphics." In: *Computational Materials Science* 2.2 (1994), pp. 279–286. ISSN: 0927-0256. DOI: http://dx.doi.org/10.1016/0927-0256(94)90109-0. URL: http://www.sciencedirect.com/science/article/pii/0927025694901090.

[41]   Craig W. Reynolds. "Flocks, herds and schools: A distributed behavioral model." In: *Proceedings of the 14th annual conference on Computer graphics and interactive techniques - SIGGRAPH '87*. New York, New York, USA: ACM Press, 1987, pp. 25–34. ISBN: 0897912276. DOI: 10.1145/37401.37406. URL: http://portal.acm.org/citation.cfm?doid=37401.37406.

[42]   Frank H. Heppner and U. Grenander. "A stochastic nonlinear model for coordinated bird flocks." In: 1990.

[43]   Richard M Martin. *Electronic structure: basic theory and practical methods*. Cambridge university press, 2004, pp. 119–159.

[44]   P. Hohenberg and W. Kohn. "Inhomogeneous Electron Gas." In: *Phys. Rev.* 136 (3B Nov. 1964), B864–B871. DOI: 10.1103/PhysRev.136.B864. URL: https://link.aps.org/doi/10.1103/PhysRev.136.B864.

[45]   E. Engel and R.M. Dreizler. *Density Functional Theory – An Advanced Course*. Springer-Verlag Berlin Heidelberg, 2011.

[46]   W. Kohn and L. J. Sham. "Self-Consistent Equations Including Exchange and Correlation Effects." In: *Phys. Rev.* 140 (4A Nov. 1965), A1133–A1138. DOI: 10.1103/PhysRev.140.A1133. URL: https://link.aps.org/doi/10.1103/PhysRev.140.A1133.

[47]   John P Perdew and Kieron Burke. "Comparison shopping for a gradient-corrected density functional." In: *International journal of quantum chemistry* 57.3 (1996), pp. 309–319.

[48]   Per-Sverre Svendsen and Ulf von Barth. "Gradient expansion of the exchange energy from second-order density response theory." In: *Physical Review B* 54.24 (1996), p. 17402.

[49] Axel D Becke. "Density-functional exchange-energy approximation with correct asymptotic behavior." In: *Physical review A* 38.6 (1988), p. 3098.

[50] John P Perdew and Yue Wang. "Accurate and simple analytic representation of the electron-gas correlation energy." In: *Physical Review B* 45.23 (1992), p. 13244.

[51] J. P. Perdew, K. Burke, and M. Ernzerhof. "Generalized gradient approximation made simple." In: *Phys. Rev. Lett.* 77 (1996), pp. 3865–3868.

[52] Patanachai Janthon, Sijie (Andy) Luo, Sergey M. Kozlov, Francesc Viñes, Jumras Limtrakul, Donald G. Truhlar, and Francesc Illas. "Bulk Properties of Transition Metals: A Challenge for the Design of Universal Density Functionals." In: *Journal of Chemical Theory and Computation* 10.9 (2014). PMID: 26588528, pp. 3832–3839. DOI: `10.1021/ct500532v`. eprint: `http://dx.doi.org/10.1021/ct500532v`. URL: `http://dx.doi.org/10.1021/ct500532v`.

[53] Alberto Ambrosetti and Pier Luigi Silvestrelli. "Cohesive properties of noble metals by van der Waals-corrected density functional theory: Au, Ag, and Cu as case studies." In: *Phys. Rev. B* 94 (4 July 2016), p. 045124. DOI: `10.1103/PhysRevB.94.045124`. URL: `https://link.aps.org/doi/10.1103/PhysRevB.94.045124`.

[54] C. Kittel. *Introduction to Solid State Physics*. University of California, Berkeley, 2005.

[55] Sang H. Yang, David A. Drabold, James B. Adams, Pablo Ordejón, and Keith Glassford. "Density functional studies of small platinum clusters." In: *Journal of Physics: Condensed Matter* 9.5 (Feb. 1997), pp. L39–L45. ISSN: 0953-8984. DOI: `10.1088/0953-8984/9/5/002`. URL: `https://iopscience.iop.org/article/10.1088/0953-8984/9/5/002`.

[56] H. Hellmann. "A New Approximation Method in the Problem of Many Electrons." In: *The Journal of Chemical Physics* 3.1 (1935), pp. 61–61. DOI: `10.1063/1.1749559`. eprint: `http://dx.doi.org/10.1063/1.1749559`. URL: `http://dx.doi.org/10.1063/1.1749559`.

[57] Llewellyn Hilleth Thomas. "The calcuation of atomic fields." In: *Mathematical Proceedings of the Cambridge Philosophical Society* 23.5 (1927), pp. 542–548. DOI: 10.1017/S0305004100011683.

[58] Enrico Fermi. "Un metodo statistico per la determinazione di alcune proprietà dell'atomo." In: *Rend. Accad. Naz. Lincei* 6.602-607 (1927), p. 32.

[59] G. B. Bachelet, D. R. Hamann, and M. Schlüter. "Pseudopotentials that work: From H to Pu." In: *Phys. Rev. B* 26 (8 Oct. 1982), pp. 4199–4228. DOI: 10.1103/PhysRevB.26.4199. URL: https://link.aps.org/doi/10.1103/PhysRevB.26.4199.

[60] P. E. Blöchl. "Projector augmented-wave method." In: *Physical Review B* 50.24 (Dec. 1994), pp. 17953–17979. ISSN: 0163-1829. DOI: 10.1103/PhysRevB.50.17953. URL: https://link.aps.org/doi/10.1103/PhysRevB.50.17953.

[61] G. Kresse and D. Joubert. "From ultrasoft pseudopotentials to the projector augmented-wave method." In: *Physical Review B* 59.3 (Jan. 1999), pp. 1758–1775. ISSN: 0163-1829. DOI: 10.1103/PhysRevB.59.1758. URL: https://link.aps.org/doi/10.1103/PhysRevB.59.1758.

[62] V. Rosato, M. Guillope, and B. Legrand. "Thermodynamical and structural properties of f.c.c. transition metals using a simple tight-binding model." In: *Philosophical Magazine A* 59.2 (1989), pp. 321–336. DOI: 10.1080/01418618908205062. eprint: http://www.tandfonline.com/doi/pdf/10.1080/01418618908205062. URL: http://www.tandfonline.com/doi/abs/10.1080/01418618908205062.

[63] F. Cyrot-Lackmann and F. Ducastelle. "Binding Energies of Transition-Metal Atoms Adsorbed on a Transition Metal." In: *Phys. Rev. B* 4 (8 Oct. 1971), pp. 2406–2412. DOI: 10.1103/PhysRevB.4.2406. URL: https://link.aps.org/doi/10.1103/PhysRevB.4.2406.

[64] M.C. Desjonqueres and D. Spanjaard. *Concepts in Surface Physics*. Springer Berlin Heidelberg, 2012. ISBN: 9783642614002. URL: https://books.google.it/books?id=T0zuCAAAQBAJ.

[65] J. C. Slater and G. F. Koster. "Simplified LCAO Method for the Periodic Potential Problem." In: *Phys. Rev.* 94 (6 June 1954), pp. 1498–1524. DOI: 10.1103/PhysRev.

94.1498. URL: https://link.aps.org/doi/10.1103/PhysRev.94.1498.

[66] Fabrizio Cleri and Vittorio Rosato. "Tight-binding potentials for transition metals and alloys." In: *Phys. Rev. B* 48 (1 July 1993), pp. 22–33. DOI: 10.1103/PhysRevB.48.22. URL: https://link.aps.org/doi/10.1103/PhysRevB.48.22.

[67] M. P. Allen and D. J. Tildesley. *Computer Simulation of Liquids*. Clarendon, Oxford, 1987.

[68] C. Mottet, G. Tréglia, and B. Legrand. "Structures of a Ag monolayer deposited on Cu(111), Cu(100), and Cu(110) substrates: An extended tight-binding quenched-molecular-dynamics study." In: *Phys. Rev. B* 46 (1992), p. 16018.

[69] F. Baletto, C. Mottet, and R. Ferrando. "Growth simulations of silver shells on copper and palladium nanoclusters." In: *Phys. Rev. B* 66 (2002), p. 155420.

[70] William L. Jorgensen, David S. Maxwell, and Julian Tirado-Rives. "Development and Testing of the OPLS All-Atom Force Field on Conformational Energetics and Properties of Organic Liquids." In: *Journal of the American Chemical Society* 118.45 (Jan. 1996), pp. 11225–11236. ISSN: 0002-7863. DOI: 10.1021/ja9621760. URL: https://pubs.acs.org/doi/10.1021/ja9621760.

[71] Paul Wynblatt. "A calculation of the surface energies of fcc transition metals." In: *Surface Science* 136.2 (1984), pp. L51–L56. ISSN: 0039-6028. DOI: https://doi.org/10.1016/0039-6028(84)90608-3. URL: https://www.sciencedirect.com/science/article/pii/0039602884906083.

[72] D. Alloyeau, C. Ricolleau, C. Mottet, T. Oikawa, C. Langlois, Y. Le Bouar, N. Braidy, and A. Loiseau. "Size and shape effects on the order-disorder phase transition in CoPt nanoparticles." In: *Nature Materials* 8 (2009), pp. 940–946.

[73] Ph. Borel and J.-P. Buffat. "Size effect on the melting temperature of gold partlcles." In: *Phys. Rev. A* 13 (1976), pp. 2287–2298.

[74] Ph. Durussel and P. Feschotte. "A revision of the binary system Ag-Pt." In: *Journal of Alloys and Compounds* 239.2 (1996), pp. 226–230.

[75]   Paolo Giannozzi et al. "QUANTUM ESPRESSO: a modular and open-source software project for quantum simulations of materials." In: *Journal of Physics: Condensed Matter* 21.39 (Sept. 2009), p. 395502. ISSN: 0953-8984. DOI: 10.1088/0953-8984/21/39/395502. URL: https://iopscience.iop.org/article/10.1088/0953-8984/21/39/395502.

[76]   David Vanderbilt. "Soft self-consistent pseudopotentials in a generalized eigenvalue formalism." In: *Physical Review B* 41.11 (Apr. 1990), pp. 7892–7895. ISSN: 0163-1829. DOI: 10.1103/PhysRevB.41.7892. URL: https://link.aps.org/doi/10.1103/PhysRevB.41.7892.

[77]   Zhiqiang Shen, Mu-Ping Nieh, and Ying Li. "Decorating Nanoparticle Surface for Targeted Drug Delivery: Opportunities and Challenges." In: *Polymers* 8.3 (Mar. 2016), p. 83. ISSN: 2073-4360. DOI: 10.3390/polym8030083. URL: http://www.mdpi.com/2073-4360/8/3/83.

[78]   Bengt Fadeel and Alfonso E. Garcia-Bennett. "Better safe than sorry: Understanding the toxicological properties of inorganic nanoparticles manufactured for biomedical applications." In: *Advanced Drug Delivery Reviews* 62.3 (Mar. 2010), pp. 362–374. ISSN: 0169409X. DOI: 10.1016/j.addr.2009.11.008. URL: https://linkinghub.elsevier.com/retrieve/pii/S0169409X09003469.

[79]   Bei Zhang, Olga V. Safonova, Stephan Pollitt, Giovanni Salassa, Annelies Sels, Rania Kazan, Yuming Wang, Günther Rupprechter, Noelia Barrabés, and Thomas Bürgi. "On the mechanism of rapid metal exchange between thiolate-protected gold and gold/silver clusters: a time-resolved in situ XAFS study." In: *Physical Chemistry Chemical Physics* 20.7 (2018), pp. 5312–5318. ISSN: 1463-9076. DOI: 10.1039/C7CP08272J. URL: http://xlink.rsc.org/?DOI=C7CP08272J.

[80]   Hannu Häkkinen. "The gold–sulfur interface at the nanoscale." In: *Nature Chemistry* 4.6 (June 2012), pp. 443–455. ISSN: 1755-4330. DOI: 10.1038/nchem.1352. URL: http://dx.doi.org/10.1038/nchem.1352%20http://www.nature.com/articles/nchem.1352.

[81]   Robert L. Whetten and Ryan C. Price. "CHEMISTRY: Nano-Golden Order." In: *Science* 318.5849 (Oct. 2007), pp. 407–408. ISSN: 0036-8075. DOI: 10.1126/science.

1150176. URL: https://www.sciencemag.org/lookup/doi/10.1126/science.1150176.

[82] Frank Schreiber. "Structure and growth of self-assembling monolayers." In: *Progress in Surface Science* 65.5-8 (Nov. 2000), pp. 151–257. ISSN: 00796816. DOI: 10.1016/S0079-6816(00)00024-1. URL: https://linkinghub.elsevier.com/retrieve/pii/S0079681600000241.

[83] Ani Baghdasaryan, Kévin Martin, Latévi Max Lawson Daku, Maurizio Mastropasqua Talamo, Narcis Avarvari, and Thomas Bürgi. "Ligand exchange reactions on the chiral Au 38 cluster: CD modulation caused by the modification of the ligand shell composition." In: *Nanoscale* 12.35 (2020), pp. 18160–18170. ISSN: 2040-3364. DOI: 10.1039/D0NR03824E. URL: http://xlink.rsc.org/?DOI=D0NR03824E.

[84] Zhi Luo, Jing Hou, Laure Menin, Quy Khac Ong, and Francesco Stellacci. "Evolution of the Ligand Shell Morphology during Ligand Exchange Reactions on Gold Nanoparticles." In: *Angewandte Chemie International Edition* 56.43 (Oct. 2017), pp. 13521–13525. ISSN: 14337851. DOI: 10.1002/anie.201708190. URL: http://doi.wiley.com/10.1002/anie.201708190.

[85] Stefania Sabella et al. "A general mechanism for intracellular toxicity of metal-containing nanoparticles." In: *Nanoscale* 6.12 (2014), p. 7052. ISSN: 2040-3364. DOI: 10.1039/c4nr01234h. URL: http://xlink.rsc.org/?DOI=c4nr01234h.

[86] D. Porezag, Th. Frauenheim, Th. Köhler, G. Seifert, and R. Kaschner. "Construction of tight-binding-like potentials on the basis of density-functional theory: Application to carbon." In: *Physical Review B* 51.19 (May 1995), pp. 12947–12957. ISSN: 0163-1829. DOI: 10.1103/PhysRevB.51.12947. URL: https://link.aps.org/doi/10.1103/PhysRevB.51.12947.

[87] G. Seifert, D. Porezag, and Th. Frauenheim. "Calculations of molecules, clusters, and solids with a simplified LCAO-DFT-LDA scheme." In: *International Journal of Quantum Chemistry* 58.2 (1996), pp. 185–192. ISSN: 0020-7608. DOI: 10.1002/(SICI)1097-461X(1996)58:2<185::AID-QUA7>3.0.CO;2-U. URL: https://onlinelibrary.wiley.com/doi/10.1002/(SICI)1097-461X(1996)58:2%7B%5C%%7D3C185::AID-QUA7%7B%5C%%7D3E3.0.CO;2-U.

[88] M. Elstner, D. Porezag, G. Jungnickel, J. Elsner, M. Haugk, Th. Frauenheim, S. Suhai, and G. Seifert. "Self-consistent-charge density-functional tight-binding method for simulations of complex materials properties." In: *Physical Review B* 58.11 (Sept. 1998), pp. 7260–7268. ISSN: 0163-1829. DOI: 10.1103/PhysRevB.58.7260. URL: https://link.aps.org/doi/10.1103/PhysRevB.58.7260.

[89] Ville Mäkinen, Pekka Koskinen, and Hannu Häkkinen. "Modeling thiolate-protected gold clusters with density-functional tight-binding." In: *European Physical Journal D* 67.2 (2013), pp. 1–6. ISSN: 14346060. DOI: 10.1140/epjd/e2012-30486-4.

[90] Adri C.T. Van Duin, Siddharth Dasgupta, Francois Lorant, and William A. Goddard. "ReaxFF: A reactive force field for hydrocarbons." In: *Journal of Physical Chemistry A* 105.41 (2001), pp. 9396–9409. ISSN: 10895639. DOI: 10.1021/jp004368u.

[91] Thomas P. Senftle et al. "The ReaxFF reactive force-field: Development, applications and future directions." In: *npj Computational Materials* 2.September 2015 (2016). ISSN: 20573960. DOI: 10.1038/npjcompumats.2015.11.

[92] Emmi Pohjolainen, Xi Chen, Sami Malola, Gerrit Groenhof, and Hannu Häkkinen. "A Unified AMBER-Compatible Molecular Mechanics Force Field for Thiolate-Protected Gold Nanoclusters." In: *Journal of Chemical Theory and Computation* 12.3 (Mar. 2016), pp. 1342–1350. ISSN: 1549-9618. DOI: 10.1021/acs.jctc.5b01053. URL: https://pubs.acs.org/doi/10.1021/acs.jctc.5b01053.

[93] Susanna Monti, Vincenzo Carravetta, and Hans Ågren. "Simulation of Gold Functionalization with Cysteine by Reactive Molecular Dynamics." In: *The Journal of Physical Chemistry Letters* 7.2 (Jan. 2016), pp. 272–276. ISSN: 1948-7185. DOI: 10.1021/acs.jpclett.5b02769. URL: https://pubs.acs.org/doi/10.1021/acs.jpclett.5b02769.

[94] Susanna Monti, Giovanni Barcaro, Luca Sementa, Vincenzo Carravetta, and Hans Ågren. "Characterization of the adsorption dynamics of trisodium citrate on gold in water solution." In: *RSC Advances* 7.78 (2017), pp. 49655–49663. ISSN: 20462069. DOI: 10.1039/c7ra10759e.

[95]   Susanna Monti, Vincenzo Carravetta, and Hans Ågren. "Decoration of gold nanoparticles with cysteine in solution: reactive molecular dynamics simulations." In: *Nanoscale* 8.26 (2016), pp. 12929–12938. ISSN: 2040-3364. DOI: 10.1039/C6NR03181A.

[96]   Francesca Baletto and Riccardo Ferrando. "Structural properties of nanoclusters: Energetic, thermodynamic, and kinetic effects." In: *Rev. Mod. Phys.* 77 (2005), pp. 371–423.

[97]   Louise B. Wright, P. Mark Rodger, Stefano Corni, and Tiffany R. Walsh. "GolP-CHARMM: First-Principles Based Force Fields for the Interaction of Proteins with Au(111) and Au(100)." In: *Journal of Chemical Theory and Computation* 9.3 (Mar. 2013), pp. 1616–1630. ISSN: 1549-9618. DOI: 10.1021/ct301018m. URL: https://pubs.acs.org/doi/10.1021/ct301018m.

[98]   F. Iori, R. Di Felice, E. Molinari, and S. Corni. "GolP: An atomistic force-field to describe the interaction of proteins with Au(111) surfaces in water." In: *Journal of Computational Chemistry* 30.9 (July 2009), pp. 1465–1476. ISSN: 01928651. DOI: 10.1002/jcc.21165. URL: http://doi.wiley.com/10.1002/jcc.21165.

[99]   Guobing Zhou, Chang Liu, Lloyd A. Bumm, and Liangliang Huang. "Force Field Parameter Development for the Thiolate/Defective Au(111) Interface." In: *Langmuir* 36.15 (2020), pp. 4098–4107. ISSN: 15205827. DOI: 10.1021/acs.langmuir.0c00530.

[100] M. M. Mariscal, J. A. Olmos-Asar, C. Gutierrez-Wing, A. Mayoral, and M. J. Yacaman. "On the atomic structure of thiol-protected gold nanoparticles: a combined experimental and theoretical study." In: *Physical Chemistry Chemical Physics* 12.37 (2010), p. 11785. ISSN: 1463-9076. DOI: 10.1039/c004229c. URL: http://xlink.rsc.org/?DOI=c004229c.

[101] Hendrik Heinz, R a Vaia, B L Farmer, and R R Naik. "Accurate Simulation of Surfaces and Interfaces of Face-Centered Cubic Metals Using 12- 6 and 9- 6 Lennard-Jones Potentials." In: *J. Phys. Chem. C* 112.44 (2008), pp. 17281–17290. ISSN: 1932-7447. DOI: 10.1021/jp801931d. URL: http://pubs.acs.org/doi/abs/10.1021/jp801931d.

[102]   Peter Maksymovych, Oleksandr Voznyy, Daniel B. Dougherty, Dan C. Sorescu, and John T. Yates. "Gold adatom as a key structural component in self-assembled monolayers of organosulfur molecules on Au(111)." In: *Progress in Surface Science* 85.5-8 (May 2010), pp. 206–240. ISSN: 00796816. DOI: 10.1016/j.progsurf.2010.05.001. URL: http://dx.doi.org/10.1016/j.progsurf.2010.05.001%20https://linkinghub.elsevier.com/retrieve/pii/S0079681610000122.

[103]   Daniele Rapetti and Riccardo Ferrando. "Density functional theory global optimization of chemical ordering in AgAu nanoalloys." In: *Journal of Alloys and Compounds* 779 (Mar. 2019), pp. 582–589. ISSN: 09258388. DOI: 10.1016/j.jallcom.2018.11.143. URL: https://doi.org/10.1016/j.jallcom.2018.11.143%20https://linkinghub.elsevier.com/retrieve/pii/S092583881834266X.

[104]   Ali Kemal Garip, Haydar Arslan, Daniele Rapetti, and Riccardo Ferrando. "A DFT study of chemical ordering and oxygen adsorption in AuPtPd ternary nanoalloys." In: *Materials Today Communications* 25.May (Dec. 2020), p. 101545. ISSN: 23524928. DOI: 10.1016/j.mtcomm.2020.101545. URL: https://doi.org/10.1016/j.mtcomm.2020.101545%20https://linkinghub.elsevier.com/retrieve/pii/S2352492820325563.